

## Hydrothermal activity along a strike-slip fault zone and host units in the São Francisco Craton, Brazil – Implications for fluid flow in sedimentary basins

Cazarin, C. L.; van der Velde, R.; Santos, R. V.; Reijmer, J. J.G.; Bezerra, F. H.R.; Bertotti, G.; La Bruna, V.; Silva, D. C.C.; de Castro, D. L.; Srivastava, N. K.

**DOI**

[10.1016/j.precamres.2021.106365](https://doi.org/10.1016/j.precamres.2021.106365)

**Publication date**

2021

**Document Version**

Accepted author manuscript

**Published in**

Precambrian Research

**Citation (APA)**

Cazarin, C. L., van der Velde, R., Santos, R. V., Reijmer, J. J. G., Bezerra, F. H. R., Bertotti, G., La Bruna, V., Silva, D. C. C., de Castro, D. L., Srivastava, N. K., & Barbosa, P. F. (2021). Hydrothermal activity along a strike-slip fault zone and host units in the São Francisco Craton, Brazil – Implications for fluid flow in sedimentary basins. *Precambrian Research*, 365, Article 106365. <https://doi.org/10.1016/j.precamres.2021.106365>

**Important note**

To cite this publication, please use the final published version (if applicable). Please check the document version above.

**Copyright**

Other than for strictly personal use, it is not permitted to download, forward or distribute the text or part of it, without the consent of the author(s) and/or copyright holder(s), unless the work is under an open content license such as Creative Commons.

**Takedown policy**

Please contact us and provide details if you believe this document breaches copyrights. We will remove access to the work immediately and investigate your claim.

27 **Abstract**

28 This study combines multiscale analyses of geological, fault, fracture, and stable  
29 isotope data to investigate strike-slip deformation and channeling of  
30 hydrothermal fluids along the Cafarnaum fault and calcite veins at different  
31 distances from the fault, which is a structure in the São Francisco Craton,  
32 northeastern Brazil. Meteoric fluids with  $\delta D$  values near  $-45\text{‰}$  and  $\delta^{18}O$  values  
33 near  $-6.5\text{‰}$  and temperatures at  $40\text{-}70^\circ\text{C}$  precipitated as calcite veins in the host  
34 carbonate units. The Cafarnaum fault, a N-S-striking vertical,  $\sim 170$  km long fault  
35 zone, juxtaposes Neoproterozoic carbonate rocks in the western block and  
36 Mesoproterozoic siliciclastic rocks in the eastern block. A zone of restraining  
37 bends occurs at the central part of the fault, whereas termination zones of  
38 horsetail geometry occur at both ends of the Cafarnaum fault. These zones are  
39 marked by NW-SE-striking extensional faults that are oblique to the main N-S-  
40 striking fault zone, where hydrothermal deposits occur. The zone of influence of  
41 the Cafarnaum fault is  $\sim 20$  km wide around the main fault. The fault formed  
42 during the Brasiliano orogeny (740-560 Ma) after Neoproterozoic carbonate  
43 platform deposition. In contrast with the host units, fluids along the fault zone  
44 originated in deeper levels of the crust and show much lower  $\delta^{18}O$  values,  
45 indicating higher crystallization temperatures. These fluids caused brecciation in  
46 the Neoproterozoic carbonate host rocks, whereas a subsequent decrease in  
47 fluid pressure and cooling near the surface resulted in the precipitation of a  
48 hydrothermal paragenesis in veins, also affecting the host rock.

49

50 **Keywords:** carbonate veins, hydrothermal fluid, strike-slip fault, Salitre  
51 Formation, São Francisco Craton

52

## 53 1. Introduction

54 Sedimentary basins display different fluid migration regimes depending on  
55 the host rock, particularly in areas subjected to extensional tectonics.  
56 Sedimentary stratified layers may allow basinal fluids to migrate laterally parallel  
57 to bedding for hundreds of kilometers (Qing and Mountjoy, 1992). In most  
58 instances, sedimentary basins display limited vertical fluid flow due to  
59 impermeable layers; hence, fluid conduits cannot connect deep and shallow parts  
60 of a basin. Pore water usually has a low-velocity flow regime, and its primary  
61 geochemical values are therefore easily altered by reactions with host rock  
62 minerals and mixing with other fluids (Bjorlykke and Egeberg, 1993).

63 Vertical fluid flow pathways in sedimentary basins are associated with fault  
64 zones (Haneberg et al., 1999; Hardebeck and Hauksson, 1999). Depending on  
65 the structures and/or permeability properties, fault zones can either act as  
66 hydraulic barriers or as preferential conduits for geofluid migration  
67 (Gudmundsson, 2001; Rawling et al., 2001; Smeraglia et al., 2021; La Bruna et  
68 al., 2021). These characteristics are also linked to the several  
69 structural/diagenetic phases affecting the carbonate rocks from the earliest  
70 diagenetic stages (e.g., La Bruna et al., 2020). In fact, selective cementation  
71 and structural diagenetic processes are key factors in fault permeability control  
72 (Hausegger et al., 2010; Ngwenya et al., 2000).

73 Strike-slip faults create complex and heterogeneous permeability  
74 anisotropy and strongly influence fluid migration in crustal fault zones (Caine et  
75 al., 2010; Bense et al., 2013; Arancibia et al., 2014). A wide variety of processes  
76 at various scales can occur during fault growth and lead to a large range of fault  
77 architectures and properties that influence fluid flow behavior (Wibberley and

78 [Shipton, 2010](#)). The activity of major and weak strike-slip fault systems is  
79 influenced by fluid flow (e.g., [Byerlee, 1990](#); [Rice, 1992](#); [Sleep and Blanpied,](#)  
80 [1992](#); [Evans and Chester, 1995](#); [Zhang et al., 2001](#)). The internal structure of  
81 strike-slip faults is dominated by vein arrays and hydraulic breccias. These  
82 features result from intense, deep-seated, and localized hydrothermal fluid flow  
83 ([Cox and Munroe, 2016](#)). Fluid flow history can be investigated in exhumed faults  
84 and fractures, which provide information about deformation mechanisms, fluid-  
85 rock interactions, and bulk chemical redistributions ([Arancibia et al., 2014](#);  
86 [Steyrer and Sturm, 2002](#)). Among other features, synthetic faults, antithetic faults,  
87 deformation bands, joints, stylolites, veins, and breccia have been recognized in  
88 strike-slip fault zones affected by hydrothermal fluids (e.g., [Fossen and Rotevatn,](#)  
89 [2016](#); [Choi et al., 2016](#); [Liao et al., 2017](#); [Peacock et al., 2017a, 2017b](#); [Alsop et](#)  
90 [al., 2020](#); [Ostermeijer et al., 2020](#)). However, there is a debate about which of  
91 these structures, if any, exerts a primary influence on fluid flow and the role and  
92 origin of fluids in strike-slip fault zones (e.g., [Gudmundsson et al., 2002](#);  
93 [Gudmundsson, 2007](#)).

94 Several studies show that hydrothermal deposits occur in the São Francisco  
95 Craton region, including those around fault zones, while the region remained  
96 tectonically stable during the Brasiliano/Panafrican orogenic cycle at 740-540 Ma  
97 (e.g., [Almeida et al., 2000](#); [Brito Neves et al., 2014](#)). This study focuses on the  
98 Cafarnaum fault zone, which occurs as a lateral ramp ([Fig. 1A, B, C, D](#)). However,  
99 the relationship between the location and timing of hydrothermal deposit  
100 formation and fault geometry and evolution remains elusive.

101         This study is a multiscale and multidisciplinary approach that uses remote  
102 sensing, aeromagnetic data, field observations, petrography, and stable isotope  
103 geochemistry to compare the structural evolution of the hydrothermal system in

104 the siliciclastic and carbonate host rocks along the Cafarnaum fault zone and the  
105 inner basin. We present stable isotope analyses on carbonate host rocks, veins,  
106 pockets, and fluid inclusions of the inner basin to reconstruct fluid-rock  
107 interactions and build a model to predict the development of hydrothermal activity  
108 on a regional scale, which can be used as a proxy for other basins elsewhere.  
109 New stable isotope data of fluid inclusions and veins and previously published  
110 data of sulfur in sulfides show that carbonate veins associated with fractures at  
111 the edge of the basin record much higher temperatures than those crystallized in  
112 the central part of the basin. This study also describes and discusses the  
113 kinematics, morphology, and magnetic characteristics of the fault zone and the  
114 formation of various types of hydrothermal dilation breccias in the damage zone.  
115 Finally, a comparison of the Precambrian Cafarnaum fault system and its host  
116 rocks with other faults that affect other carbonate and siliciclastic units helps  
117 understand regional predictability. This study concludes that fluid flow occurs  
118 mainly along extensional subsidiary faults and investigates the way they deform  
119 the host rocks. The isotope data indicate that fluids are meteoric in origin and,  
120 compared to the sedimentary basins, fluids that percolated the crystalline terrain  
121 may have circulated into much deeper zones.

## 122 **2. Geological setting**

123 The study area is mainly composed of Mesoproterozoic rocks of the  
124 Chapada Diamantina Group and Neoproterozoic units of the Una Group,  
125 primarily the Salitre Formation (Fig. 1D, E ). The groups contain distinct  
126 formations and contrasting structural styles. Both major terrains are bounded by  
127 a strike-slip fault that we name the Cafarnaum fault in this study. It acted as a  
128 tectonic boundary between the aforementioned Mesoproterozoic and  
129 Neoproterozoic units (La Bruna et al., 2021).

130 The Chapada Diamantina Group is 1,000 m thick and includes the Morro  
131 do Chapéu Formation, which was deposited at ~1400-900 Ma ([Pedreira et al.,](#)  
132 [1975](#); [D'Angelo et al., 2020](#)). This unit was affected by a first contractional  
133 inversion event that is mainly marked by symmetrical, N-S-trending, open folds  
134 ([Danderfer et al., 2015](#); [D'Angelo et al., 2020](#)). High-angle fractures strike mostly  
135 N-S, NE-SW and NW-SE, and have a high degree of symmetry with the N-S  
136 regional folds ([Danderfer et al., 2015](#)).

137 The Salitre Formation is ~750 m thick in the central part of the Irecê Basin  
138 ([D'Angelo et al., 2020](#)), which was deposited in a carbonate pelitic marine basin  
139 ([Misi et al. 2005, 2011](#)) at ~750 Ma ([D'Angelo et al., 2020](#)). This sequence was  
140 deposited in the Irecê Basin, an asymmetric graben with an approximately N-S-  
141 oriented axis that plunges toward the north ([Lagoeiro, 1990](#); [Kuchenbecker et al.,](#)  
142 [2011](#); [Brito Neves et al., 2012](#); [D'Angelo et al., 2020](#)). The Irecê Basin was  
143 inverted in the Brasiliano orogeny, with a peak at ~600 Ma, which resulted in  
144 anomalous deformation concerning adjacent domains, with a series of south-  
145 verging fold and thrust systems ([Lagoeiro, 1990](#); [Teixeira et al., 2019](#); [D'Angelo](#)  
146 [et al., 2020](#)).

147 The carbonate units of the Irecê Basin have similar Pb-Pb isochron ages and  
148 paleomagnetic poles, which fall close to ~520 Ma. This age is consistent with the  
149 Gondwana supercontinent's apparent polar wander path and indicates that  
150 isotopic and magnetic systems reset those of the Cambrian ([Trindade et al.,](#)  
151 [2004](#)). This event was related to regional-scale fluid migration and subsequent  
152 mineralization at the end of the Brasiliano orogenic cycle ([Trindade et al., 2004](#)).

153 An E-W-oriented magnetic telluric section across the Irecê and Morro do  
154 Chapéu Basins reveals lithospheric resistive blocks bounded by major conductive

155 deep zones, which are interpreted as faults. It shows that a lithospheric  
156 conductor, interpreted as a suture zone, occurs between the Neoproterozoic  
157 Irecê Basin and the Chapada Diamantina Group (Fig. 1D ). The high  
158 conductance zone is a combination of high porosity and high fluid salinity (Padilha  
159 et al., 2019).

160 Detailed geological mapping on both sides of the fault indicates a great  
161 number of occurrences of hydrothermal minerals associated with faults. These  
162 occurrences encompass metals such as Au, Pb-Zn, and Ba. These metals occur  
163 in sulfides associated with quartz veins in dolomite units close to the main faults.  
164 In a few cases, minerals such as barite also occur in the host carbonate rocks  
165 (Sampaio et al., 2001).

166 More detailed studies have also investigated hydrothermal silicification  
167 and dolomitization in a few karst systems. Several works, conducted in the São  
168 Francisco Craton, have already investigated cave geometry, stratigraphy,  
169 geochemistry, and mineralogy to indicate that fault and fracture systems were  
170 used as conduits for deep-seated fluid flow (Klimchouk et al., 2016; Cazarin et  
171 al., 2019; La Bruna et al., 2021; Pontes et al., 2021). In another case,  
172 approximately 100 km to the south of the study area, a N-S-striking, strike-slip  
173 fault in the southern part of the Irecê Basin was the pathway for fluid flow confined  
174 to the Salitre Formation during the Brasiliano orogeny. The first stage of Mg-  
175 rich fluids caused extensive dolomitization in the Salitre Formation, which was  
176 subsequently followed by Si-rich fluids that caused pervasive silicification in the  
177 host units (Bertotti et al., 2020).

178

179 **3. Methods**

180 The present study integrates (1) remote sensing and structural investigation, (2)  
181 Geophysical data and processing, (3) sampling, (4) mineralogy and petrography,  
182 (5) stable isotope analysis of veins and host rock, and (6) isotope geochemistry  
183 of fluid inclusions. We used the Shuttle Radar Topographic Mission (SRTM),  
184 ALOS-PALSAR to map regional structures, and unmanned aerial vehicle imagery  
185 for a detailed investigation of tectonic features (Fig. 2). The aeromagnetic data  
186 used to map fault segments are from the Centro Norte Bahia Project is an  
187 airborne magnetic survey carried out by Companhia Baiana de Pesquisa Mineral  
188 (CBPM) (Fig. 3). The petrography, mineralogy, isotope, and fluid inclusions are  
189 based on the analysis of six outcrops in carbonate units of the Salite Formation  
190 on both sides of the Cafarnaum fault. We present a complete description of data  
191 and methods in the supporting material section (Methods – supporting material).

192

## 193 **4. Results**

### 194 *4.1 Qualitative field fracture analysis*

195 Different fracture types were distinguished; joints display their peculiar plumose  
196 morphology (Pollard and Aydin, 1988), and are compartmentalized or not within  
197 single beds (Fig. 4 ). For this reason, they are here named stratabound (SB) and  
198 non-stratabound (NSB) fractures. Veins are also SB and NSB, but in some  
199 outcrops they are subvertical and parallel to the tilted bed layers (Fig. 4C, D and  
200 F). Clustered fracture and vein networks were in the proximity of fault zones (Fig.  
201 5B,C, D and E). In particular, the high-resolution qualitative structural analysis  
202 shows the following fracture sets: subvertical NW-SE fractures and veins (Fig.  
203 4G, H and Fig.5B,C, D, E, F, G and H); minor subvertical NE-SW fractures and  
204 veins (Fig. 4G and Fig.5B,C, D, E, F, G and H); minor subvertical N-S fractures



205 and veins (Fig.5C, D, and F); and subvertical E-W bed-parallel veins (Fig. 4C, D  
206 and F).

207

#### 208 4.2 *Macroscale geometry and kinematics of the Cafarnaum fault*

209 The compiled structural map presents the primary structural alignments in  
210 an area of 38,000 km<sup>2</sup> (Figs. 2A, B, C, 3A, B). The tectonic structures were sorted  
211 into strike-slip faults, normal faults, reverse faults, and fold hinges based upon  
212 new original data interpretation and previous geological mapping (Cazarin et al.,  
213 2019; D'Angelo et al., 2019; Ennes-Silva et al., 2015; Souza et al., 2003). The  
214 satellite alignments were divided into the following three fault sets: NNE-SSW,  
215 NE-SW, and NW-SE. The NNE-SSW set is generally associated with strike-slip  
216 left-lateral faults, as already presented by D'Angelo et al. (2019) and Danderfer  
217 Filho et al. (2015). A zone of restraining bends coincides with an uplifted area  
218 (Fig. 2A). Additionally, drag folds occur on the west side of the Cafarnaum fault.  
219 The folded structures are E-W-striking thrusts of the Irecê Basin that bend where  
220 they reach the Cafarnaum fault. Bed layers associated to these thrust faults were  
221 tilted to the subvertical position (Fig. 4A). In some case, the aforementioned  
222 subvertical bed interfaces were affected by shearing as displayed by several  
223 kinematics indicators (Fig. 4B). Many mineralized portions documented as bed  
224 parallel veins occur along bed interlayers (Fig. 4C, D and F). Some of the thrust  
225 faults display drag folds as they approach the Cafarnaum fault. In contrast, the  
226 NE-SW- and E-W-oriented sets are composed of reverse faults, as shown by  
227 D'Angelo et al. (2019) and Reis et al. (2013).

228 The NW-SE fault set has been interpreted as composed of normal faults  
229 (D'Angelo et al., 2019). Termination zones of horsetail geometry occur at both

230 ends of the Cafarnaum fault (Fig. 2C). A few minor faults associated with veins  
231 and breccia bodies also occur at the central part of the fault zone, as at the MAM  
232 site (Fig. 5). These zones are marked by NW-SE-striking extensional faults  
233 located at the extensional quadrant of the main N-S-striking fault zone (La Bruna  
234 et al., 2021). There, hydrothermal deposits concentrate on a 20 km wide zone on  
235 both sides of the central fault (Fig. 2A, C). Several hydrothermal minerals (e.g.,  
236 barite, galena) were documented in the Mam outcrop (Fig. 5B, C, D and E). In  
237 these sites, complex vein/fracture networks were observed. Both veins and  
238 fractures form a principal NW-SE striking set and a minor NE-SW set.

239 Both the NE-SW- and NW-SE-striking fault sets terminate against the  
240 NNE-SSW- to N-S-striking fault set. Eastward from the Cafarnaum fault, a larger  
241 folded zone was documented (Fig. 2B, C). Previous works have described how  
242 this sector is affected by several anticlines and synclines (Cazarin et al., 2019;  
243 D'Angelo et al., 2019; Danderfer Filho et al., 2015; Ennes-Silva et al., 2015;  
244 Souza et al., 2003). The fold hinges mainly trend along the NNE-SSW to N-S  
245 directions (Fig. 2B, C).

246 An area of ca. 14,000 km<sup>2</sup> was analyzed for structural magnetic lineament  
247 map characterization (Fig. 3A, B). The 2,818 documented lineaments were sorted  
248 into I-order, II-order, and III order lineaments. The I-order lineaments are related  
249 to regional-scale magnetic features and are composed of a major NE-SW set and  
250 minor sets striking N-S and E-W, respectively. The II-order lineaments are  
251 characterized by a major NE-SW lineament and a minor NW-SE to WNW-ESE  
252 set associated with secondary magnetic anomalies. Both I- and II-order  
253 lineaments are crosscut by the III order lineaments.

254           The III order lineaments exhibit a singular magnetic pattern, distinguished  
255 by striking high-amplitude magnetic lineaments with the extension of dozens of  
256 kilometers (Figs. 3A, B). They occur isolated or comprising sets with main NW-  
257 SE and minor NE-SW orientations. Sometimes, they are stepwise segmented (en  
258 echelon) and shifted by hundreds of meters. They truncate other magnetic  
259 lineaments in high to moderate angles, indicating a more recent geological event.  
260 Due to high magnetization contrast with bedrocks, linear and extensive  
261 waveform, and sparse spatial distribution, we associate these magnetic  
262 lineaments with mafic dikes as many authors elsewhere (e.g., Schwarz et al.,  
263 1987; Demarco et al., 2020). In fact, the NNW-SSE trending Chapada Diamantina  
264 mafic dike swarm is intrusive into the Mesoproterozoic sedimentary sequences  
265 of the Espinhaço Supergroup within the Paramirim Aulacogen (Brito, 2008;  
266 Silveira et al., 2013). The magnetite-bearing dikes are fine to medium-grained  
267 diabases. Recently Pessano et al. (2021) associated NW-SE oriented magnetic  
268 anomalies in the central portion of the São Francisco Craton with  
269 Mesoproterozoic dikes of the Chapada Diamantina swarm.

270

#### 271 4.3 - *Hydrothermal vein and breccia characterization*

272           Two main types of structures related to hydrothermal activity occur in the  
273 Cafarnaum fault zone and its surroundings. The first type is hydrothermal  
274 breccias, which mainly occur in dilational jogs. The second is calcite veins, which  
275 are widespread in the fault zone and the host rocks away from the fault. Two sites  
276 of hydrothermal breccias occur along NW-SE striking extensional faults, which  
277 we describe below. In addition, we describe four sites with calcite veins at varying  
278 distances from the Cafarnaum fault.

279 Hydrothermal breccias are characterized by the interaction between rocks  
280 and hydrothermal solutions and are geometrically characterized by several  
281 parameters, such as morphology, particle size distribution, fabric, and expansion  
282 radius (Jébrak, 1997). Chemical and physical mechanisms can form these  
283 breccia bodies: the first by selective dissolution and the second by the excess  
284 tension exerted, which exceeds the tensile resistance of the material, or in some  
285 combination. The analyzed bodies are classified as mosaic breccias that are  
286 formed by fluid-assisted breach (hydraulic fracturing) using the classification  
287 given by Jebrák (1984b). Carbonate clasts are present, and clasts that are larger  
288 than 2 mm range between 60-75% of clasts and 75-100% of clasts.

289 Hydraulic breccias are rocks composed of angular to subangular  
290 fragments of dimensions ranging from 0.4 cm to 5 cm that are cut by several  
291 generations of fractures and veins. The fragments are present throughout the  
292 breccia bodies and are derived from adjacent rocks. Generally, they are  
293 monolithologic and represented by carbonate rocks corresponding to the Salitre  
294 Formation.

295 Carbonates also contain calcite and quartz geodes surrounded by intense  
296 oxidation (limonitization). The interfragmentary filling is composed of iron oxide  
297 or quartz and calcite cement. The oxidized matrix is probably formed to replace  
298 rich materials in iron from the cementing fluid. Quartz is associated with calcite,  
299 galena, and malachite. There is intense veining by a network of veins with a  
300 branched structure that range from millimeters to centimeters thick and reach  
301 30% of the total volume, and calcite veins of lesser thickness are related to quartz  
302 veins.

303 The description of carbonates can be compared to descriptions made by  
304 Souza et al. (1993), such as the association of intensely closed algal laminites  
305 corresponding to the Nova América inferior subunit (transgressive cycle III) at the  
306 MEL site, as well as area descriptions by Misi (1975) of fine dolomites with  
307 ankerite, barite and galena and light dolomites with millimeter bands, calcite  
308 impregnations and microcrystals of pyrite and galena. Nevertheless, occurrences  
309 only include sedimentary gaps along the Irecê Basin (Bonfim et al., 1985, and  
310 Souza et al., 1993).

311 The descriptions were made under transmitted light optical microscopy of  
312 the samples corresponding to MAM and MEL sites (Fig. 2A, C); the samples were  
313 divided into laminated carbonates with veins, laminated carbonates with a brittle  
314 aspect, and only the veins. The composition in these three divisions presents the  
315 same mineralogy in carbonates and the same mineralogy in the veins,  
316 differentiated by laminar and massive textural aspects in the case of carbonate  
317 alteration and fragmented textural aspects.

318

#### 319 4.4 Mineralogy, texture, and isotope geochemistry

320 Sites from the central part of the basin (SOR, IRE, and ACH) and the  
321 eastern block (FAR) (Fig. 2C) are large carbonate pavements in which primary  
322 sedimentary features are observed. Except for the FAR site, these carbonates  
323 display vertical bedding and are crosscut by centimetric calcitic veins.

324 The limestones from the SOR site consist of microbial mats. The beds are  
325 oriented subvertically within tight N-S-trending folds (Fig. 2C). Two types of veins  
326 are observed at the SOR site. The first type of veins formed on transverse fault  
327 planes, which originate in E-W-striking low-angle thrust faults, predating folding

328 to the present-day subvertical position (T16 and T19). The second type forms N-  
329 S-trending veins. These veins are associated with younger N-S shortening (T24).  
330 Isotope profiles across the veins reveal no significant difference in  $\delta^{13}\text{C}$  and  $\delta^{18}\text{O}$   
331 concentration between the carbonate host rock and the transverse fault  
332 carbonate filling (Fig. 6A-D ).

333 The FAR site (Fig. 6E-H) consists of stromatolite bioherm colonies. Two  
334 veins were analyzed. The first vein (T9) occurs in inter-stromatolite silt crosscut  
335 by a sharp-edged 2.2 mm thick vein, filled with mosaic equidimensional  
336 transparent calcite varying from 0.05 mm to 0.2 mm. The other vein (T10)  
337 crosscuts a stromatolite unit. It has two different calcite fabrics: an  
338 equidimensional mosaic with oriented sparry calcite crystals varying in size from  
339 0.1 to 1 mm and a milky white area with no calcite crystals. Most calcite veins  
340 from the FAR site display lower  $\delta^{13}\text{C}$  and  $\delta^{18}\text{O}$  values than the stromatolite host  
341 rock. Exceptions are a few carbonate samples from the vein that crosscut the  
342 inter-stromatolite silt (Fig. 6G-H).

343 The ACH site consists of subvertical NNW-dipping dolostones. The  
344 present-day NNE-SSW burial fault carries most veins and is more prominent than  
345 its conjugate NW-SE counterpart (Fig. 7A-D). Veins at the ACH site lack signs  
346 of shear and are syntaxially filled with blocky crystals. In addition to veins, the  
347 ACH site contains a pocket filled with crystal precipitates (T5) in which borders  
348 are vein wall remnants and dissolved host rock peloids (Fig. 7B-C). Since these  
349 pockets dissolve burial-related fractures and faults, they formed later than the  
350 burial fault set. In general, ACH samples show a higher porosity than other sites.  
351 Isotope data across these veins reveal much lower  $\delta^{13}\text{C}$  and  $\delta^{18}\text{O}$  values than the  
352 isotope values of the host rock (Fig. 7C-D).

353 Carbonate rocks of the IRE site consist of thinly layered (0.2-20 cm) black  
354 limestones with local slumps. The beds are vertically tilted and folded, with an  
355 orientation of 355/86 (dip azimuth direction). Two types of veins are present (Fig.  
356 97E-F): thinner (<1 cm) bedding-perpendicular and bedding-parallel pre- or  
357 synfolding veins and thick veins (20 cm) filled with a mixture of calcite and barite  
358 that irregularly crosscut folded bedding. They are syn- or post-folding veins.  
359 Similar to the SOR site veins, IRE veins have isotope values similar to the host  
360 rock (Fig. 7E-F).

361 In contrast to sites in the central part of the basin, sites at the basin edges  
362 (i.e., MEL and MAM) are strongly deformed and exhibit pervasive hydrothermal  
363 features and hydraulic hydrothermal breccias (Fig. 8A-C). Samples from the MEL  
364 site are mostly breccias with white calcite cement. Previous studies by Misi et al.  
365 (2005) argue that the Salitre Formation stratigraphy controls the Pb-Zn  
366 concentrations. According to these authors, the Pb-Zn ore is associated with  
367 silicified stromatolites that overlie a shallowing-upward sequence (Unit B1). The  
368 MEL site is located in a flat area where sites are restricted to trenches dug by  
369 mining operations. Samples may exhibit primary lamination similar to rocks of the  
370 Salitre Formation. These features are obliterated by tectonic and hydrothermal  
371 processes toward the center of the brecciated zone at the outcrop scale (Fig. 8A).  
372 Clasts of primary carbonate rocks may also occur in the hydrothermal breccia  
373 cemented by white calcite devoid of laminations (Fig. 8B). Secondary vugular-  
374 type porosity that is less than 1% in the area is also observed under the  
375 microscope. The limestones and breccias are crosscut by two generations of  
376 veins: one measuring 4 mm thick and made of calcite and, quartz microcrystals  
377 and a second measuring approximately 0.3 mm thick and made of quartz. The  
378 host carbonate and the cement display quite distinct mineralogy. The primary

379 Salitre carbonates consist mainly of calcite, dolomite, ankerite, siderite, iron  
380 oxide, and limonite. SEM, XRD, and QUEMSCAN data indicate that the veins  
381 and hydrothermal breccias display complex mineralogy, where the main minerals  
382 are calcite, dolomite, galena, barite, quartz, sphalerite, illite, chlorite, zincite,  
383 cerussite, malachite, magnesite, apatite, and chalcedony. Barite, apatite, chlorite,  
384 and quartz are concentrated along fracture zones (Fig. 8D-G) and, in some  
385 instances, may form larger aggregates. Thin section observations indicate that  
386 tectonic and hydrothermal processes were accompanied by the formation of  
387 stylolites, dolomitization, silicification, limonitization, microfractures, folding, and  
388 minerals with wavy extinction.

389 Samples (Figs.8D and E) at the MEL site display different facies of  
390 carbonate breccia and isotope  $\delta^{13}\text{C}$  and  $\delta^{18}\text{O}$  analyses performed at specific  
391 points in the samples. While the  $\delta^{13}\text{C}$  values range between 0.22‰ and -2.24‰,  
392 the  $\delta^{18}\text{O}$  values vary from -6.16‰ to -12.67‰. In most instances, the primary  
393 limestone fabric was replaced by milky carbonate with large anhedral crystals.  
394 Sample in Fig. 8C displays a cyclic succession of milky calcite and iron-rich  
395 dolomite crosscut by veins containing galena. High-resolution  $\delta^{13}\text{C}$  and  $\delta^{18}\text{O}$  data  
396 indicate that these samples may have an area with homogenous isotope values  
397 (Fig.8D-E), as well as areas with variable isotope values.

398 The MAM site is also located in a flat area in which sites are restricted to  
399 trenches of the mining operation. Centimetric veins of milky quartz occur in the  
400 carbonate host unit. As at the MEL site, XRD and SEM data at the MAM site  
401 indicate galena, zincite, ankerite, dolomite, cerussite, apatite, magnesite,  
402 anglesite, chlorite, and illite. However, in contrast to the MEL site, the MAM site  
403 exhibits strong silicification that may completely obliterate the primary carbonate  
404 texture. For instance, the QUEMSCAN images exhibit carbonate breccias



405 replaced by silica in which ghost clasts can still be identified. Pores and laminated  
406 illite and chlorite areas indicate that silica-rich fluids replaced mostly carbonate  
407 minerals

408

#### 409 *4.5 - Fluid inclusions*

410 Table 01 presents the H and O isotopic compositions of fluid inclusions for 10  
411 samples from the ACH, IRE, and SOR sites in the Irecê Basin and at the FAR  
412 site in the eastern block of the Cafarnaum fault. The supplemented materials  
413 detail linearity and memory effect corrections applied to the H and O fluid isotope  
414 data. Table 01 also shows the average  $\delta^{18}\text{O}$  isotopic composition of the carbonate  
415 associated with the fluid inclusions and the calculated temperature based on the  
416 isotope fractionation between calcite and water. The calculated temperature  
417 range is 40-74°C, with the highest values obtained in samples from the ACH and  
418 FAR sites

419 Except for one sample from the ACH site (ACH01.3Aa T5-1, left), all samples  
420 display negative  $\delta\text{D}_{\text{SMOW}}$  values. Fig. 9 plots the H and O isotope values with the  
421 global meteoric water line (GMWL) by Rozanski et al. (1993) and shows that the  
422 trending lines of samples from the ACH and FAR sites converge to a  $\delta\text{D}$  value of  
423 approximately -45‰ and a  $\delta^{18}\text{O}$  value of -6.5‰.

424

## 425 **5. Discussion**

### 426 *5.1 – Fault evolution and hydrothermal fluids*

427 Cratons are composed of thick and cool lithospheric keels with high resistivities  
428 and low porosities (e.g., Ferguson et al., 2012; Selway, 2014). However, several  
429 studies have increasingly indicated that cratons present low-resistivity zones in  
430 the lithosphere that behave as weakness zones prone to deformation, such as

431 ductile shear zones and faults (e.g., [Pinto et al., 2010](#); [Thiel and Heinson, 2013](#);  
432 [Dong et al., 2015](#)). These shear zones/faults provide a high permeability and are  
433 pathways for deep-seated fluids to ascend through the whole lithosphere ([Caine](#)  
434 [et al., 2010](#); [Bense et al., 2013](#)). The study of hydrothermal fluids in fault zones  
435 in cratons may explain the permeability of fault zones and host units and deep  
436 geothermal exploration constraints ([Taillefer et al., 2017](#)). The boundary between  
437 the Irecê Basin and the Chapada Diamantina Group is marked by the Cafarnaum  
438 fault ([Figs. 1, 2](#)) ([La Bruna et al., 2021](#)), which coincides with a high conductor  
439 mapped by a magnetotelluric survey ([Fig.10](#)). This zone was prone to  
440 hydrothermal activity and is consistent with high porosity-permeability, high-fluid  
441 salinity, and sulfide emplacement. In a few cases, it served as a conduit for mafic  
442 volcanism ([Teixeira et al., 2017](#); [Padilha et al. 2019](#)).

443         Faults behave as high permeability conduits that facilitate fluid flow in the  
444 Earth's crust ([Cox and Munroe, 2016](#)). Deep-seated hydrothermal fluids  
445 precipitate minerals that form veins and breccias and decrease the permeability  
446 of the lithospheric fault zones ([Sibson et al., 1988, 1990](#)). The precipitation of  
447 hydrothermal minerals in fault zones and host rocks is caused by decompression  
448 and cooler conditions ([Calvin et al., 2015](#)). Therefore, based on the  
449 characteristics presented here, the Cafarnaum fault was a structure prone to  
450 hydrothermal activity. It controlled the upward hot fluid flow, indicated by the  
451 relationship between fault geometry and hydrothermal deposits ([Fig.10](#)).

452         . Hydrothermal fluids channelized along faults can affect thousands of  
453 square kilometers, even in nonmagmatic settings ([Nabavi et al., 2020](#)). The  
454 hydrothermal activity in faults with shallow crustal levels under fluid overpressure  
455 is controlled by the geometry of the crustal-scale fault zone ([Bellot, 2008](#)).  
456 Dilational jogs flanking continental-scale strike-slip faults, for example, are

457 locations prone to hydrothermal boiling and implosive brecciation ([Sibson, 1987](#)).  
458 Active examples of hydrothermal activity in dilational jogs occur in compressional  
459 settings such as New Zealand ([Brathwaite et al., 1986](#) in 24) and the French  
460 Pyrenees ([Taillefer et al., 2017](#)).

461 We interpret the N-W-striking faults that arrest against the main N-S-  
462 trending Cafarnaum fault as dilational jogs that facilitate hydrothermal fluid  
463 ascension and flow ([Fig. 10](#)). Hydrothermal minerals are concentrated in dilational  
464 jogs on both sides flanking the Cafarnaum fault, either on carbonate units in  
465 the western block or mainly on siliciclastic units in the eastern block ([Fig. 2](#)). This  
466 indicates that the structure, rather than the lithology, controls the fluid flow along  
467 the fault.

468 Hydrothermal breccias occur in dilational jogs on both sides of the main  
469 Cafarnaum fault ([Fig. 2A, C](#)). These breccias form when fluid migration becomes  
470 explosive (e.g., [Jébrak, 1997](#)). Subsequent precipitation of hydrothermal minerals  
471 forms breccias and heals the fault, decreasing their permeability ([Katz et al.,](#)  
472 [2006](#); [Taillefer et al., 2017](#)). Fluid flow and subsequent precipitation have been  
473 interpreted with the seismic cycle and fault-valve behavior, influencing breccia  
474 occurrence ([Taillefer et al., 2017](#)).

475 The results shown in this study document how strike-slip faults such as the  
476 Cafarnaum fault are efficient pathways for fluids and that these fluids caused the  
477 widespread silicification and the precipitation of Ca-bearing minerals. A recently  
478 performed in the Morro Vermelho Karst System, located some 150km to the S of  
479 the Cafarnaum fault and developed within the same carbonate succession,  
480 provides more insights into the temporal succession of fluid circulation and  
481 precipitation/dissolution ([Bertotti et al., 2020](#)). During the first stage, fluids flowed  
482 along two main aquifers, the Chapada Diamantina quartz arenites and the

483 overlying Salitre Formation carbonates, separated by the Bebedouro Formation  
484 glacial sediments aquitard. The flow was associated with pervasive dolomitization  
485 of a 100s of m wide body overlying a deep-seated strike-slip fault in the  
486 carbonates. With increasing displacement, the strike-slip fault grew upward (e.g.,  
487 [Dooley and Schreurs, 2012](#)), thereby first affecting the Chapada Diamantina  
488 aquifer and eventually reaching the Salitre carbonates. With establishing a  
489 through-going fracture zone, Si-rich fluids previously confined to the Chapada  
490 Diamantina aquifer invaded the Salitre aquifer, causing widespread dissolution  
491 and karst formation and precipitation of Si both in the host rock as a silica-crust  
492 coating the caves. We suggest that such a temporal succession could also be  
493 applicable to the mineralizations of the Cafarnaum fault zone.

494

## 495 *5.2 – Geochemistry of hydrothermal fluids, fluid pathways and tectonics*

496 Fluid flow in the crust is a powerful mechanism to remobilize chemical  
497 elements and concentrate metals of economic interest ([Heinrich and Candela,](#)  
498 [2014, Yardley and Bodnar, 2014](#)).. The efficiency of heat transfer and chemical  
499 remobilization depends on heat and chemical gradients, fluid-rock interactions,  
500 and tectonic settings. Many studies have addressed the question of how deep  
501 fluid penetrates the crust (e.g., [Nesbitt and Muehlenbachs, 1989; Fricke,](#)  
502 [Wickham et al., 1992; Haines, Lynch et al., 2016](#)). Most authors agree that fluid  
503 may penetrate as deep as 10 to 15 km into the crust, mainly in crystalline terrains  
504 submitted to an extensional tectonic regime.

505 The isotope data presented here show that fluid sources in the central part  
506 and at the Irecê Basin edges had the same origin but underwent distinct  
507 pathways. The new data presented in this study allow a discussion of the source  
508 of these fluids, their primary isotopic composition, their interaction with the

509 sedimentary rocks on both sides of the Cafarnaum fault, and how deep they may  
510 have penetrated each kind of terrain.

511 Different generations of carbonate veins and breccias crosscut the  
512 sedimentary rocks of the Irecê Basin. [Figs. 6](#) and [7](#) show that carbonate  
513 veins from the central part of the basin do not display significant carbon and  
514 oxygen isotope differences relative to the carbonate host rock. More significant  
515 isotopic differences occur in samples from the ACH and FAR sites, where the  
516 veins present more negative isotopic values than the host rock ([Fig.6](#)).

517 Data in this study suggest that the  $\delta^{18}\text{O}$  value of the carbonate veins may  
518 be explained by a meteoric fluid source ([Fig.11](#)), by a higher temperature of  
519 crystallization ([Table 02](#)) of these carbonates, or by the combination of both  
520 processes. The oxygen isotope fractionation between calcite and water varies  
521 from 28‰ to 7‰ in the temperature range of 25-250°C ([Chacko et al. 1991](#); [Kim,](#)  
522 [O'Neil et al., 2007](#); [Chacko and Deines, 2008](#)). In contrast, the low  $\delta^{13}\text{C}$  values  
523 observed in the carbonate may only be explained by an external source of  
524 carbon, since the carbon isotope fractionation values between calcite and  $\text{HCO}_3^-$   
525 and calcite and  $\text{CO}_2$  are much less than 4‰ at temperatures below 200°C  
526 ([Deines et al., 1974](#); [Chacko et al., 1991](#); [Chacko and Deines 2008](#)). Samples  
527 from the MEL site, which are located at the edge of the basin, display even more  
528 negative oxygen isotope values. As shown in [Fig. 11](#), isotope data from this site  
529 display a narrow range of  $\delta^{13}\text{C}$  values and a wide range of  $\delta^{18}\text{O}$  values. Compared  
530 to the veins from the central part of the Irecê Basin, the lower  $\delta^{18}\text{O}$  values of their  
531 carbonates indicate interactions with more  $^{18}\text{O}$ -depleted fluids or higher  
532 crystallization temperatures.

533 [Fig. 11](#) compares the isotopic composition of the carbonates studied here  
534 with previous isotope data reported for the same area. The diagram shows that

535 the data in this study have a wide range of  $\delta^{18}\text{O}$  (-13.0‰ to 1.8‰) and  $\delta^{13}\text{C}$  (-  
536 10‰ to 10‰) values. However, most of our samples have a narrower range of  
537  $\delta^{13}\text{C}$  (-5‰ to 1‰). The exceptions are samples from the IRE site that exhibit  
538 higher  $\delta^{13}\text{C}$  values and a few samples from the ACH, FAR, and SOR sites that  
539 present  $\delta^{13}\text{C}$  values below -5‰. Samples from the IRE site are associated with  
540  $^{13}\text{C}$ -enriched carbonates from the upper section of the Irecê Basin and plotted as  
541 squares in [Fig. 9](#) . These primary high  $\delta^{13}\text{C}$  carbonates have been reported in  
542 both the Irecê Basin ([Misi 1988](#), [Misi and Kyle 1994](#), [Borges, Balsamo et al. 2016](#),  
543 [Caird, Pufahl et al. 2017](#)) and other Neoproterozoic basins ([Santos, Alvarenga et  
544 al. 2000](#)). Carbonate veins with  $\delta^{13}\text{C}$  values below -5‰ are probably related to  
545 the same fluid that is responsible for the carbonates that formed the calcretes  
546 previously described in the basin ([Borges, Balsamo et al. 2016](#), [Caird, Pufahl et  
547 al. 2017](#)). Published isotope data of these carbonates, plotted as "stars" in [Fig. 11](#),  
548 also present low  $\delta^{13}\text{C}$  values.

549         The source of fluids related to the carbonate veins from the central part of  
550 the Irecê Basin may be further constrained by the isotopic composition of fluid  
551 inclusions trapped in the carbonate veins. Based on the oxygen isotopic  
552 composition of these fluid inclusions and the associated carbonate, we estimate  
553 the temperature of carbonate crystallization to be between 39 and 67°C (Table  
554 02). These temperature estimates were based on Kim and O'Neil (1997) oxygen  
555 isotope fractionation equation between calcite and water. Since calcite and fluid-  
556 inclusions may be affected by post-entrapment isotope exchange during  
557 exhumation ([Nooitgedacht et al., 2021](#)), these results should indicate minimum  
558 temperature conditions. Assuming an average thermal gradient of 30 C/km, these  
559 fluids circulated at depths reaching 1000 m within the crust. [Fig. 9](#) displays the  
560 mean global meteoric water line by [Rozanski et al. \(1993\)](#) and the hydrogen and

561 oxygen isotope values of these fluid inclusions. It also shows trending lines for  
562 fluid inclusions from the ACH and FAR sites, indicating that they converge to a  
563  $\delta D$  value near  $-45\text{‰}$  and a  $\delta^{18}O$  value near  $-6.5\text{‰}$  along the mean meteoric water  
564 line (Fig. 9). We argue that these isotopic values represent the local meteoric  
565 water, which upon interaction with the host rock changed its isotopic composition  
566 along the mixing lines. A similar process has been described in active  
567 hydrothermal systems (Criss and Taylor Jr, 1986), in which there is also a more  
568 extensive range of  $\delta^{18}O$  values compared to  $\delta D$  values.

569 The isotopic variation observed in Fig. 11 may be explained by different  
570 geological scenarios. Arrows I and II represent veins formed by mixing meteoric  
571 fluids and carbonate host rocks of the inner part of the basin at low-temperature  
572 conditions (between 30 and 40°C). Arrow I indicates mixing between these fluids  
573 and carbonates from the lower section. In contrast, arrow II represents the mixing  
574 between these fluids and the  $^{13}C$ -enriched carbonates from the upper section.  
575 Arrow III represents carbonates formed by the same fluids as those of the  
576 calcretes, which have more negative  $\delta^{13}C$  values. Samples from the MEL site,  
577 represented by arrow IV, fall within the same range of  $\delta^{13}C$  values for most  
578 samples from the central part of the basin. However, they also have more  
579 negative  $\delta^{18}O$  values, indicating that isotope exchange between the meteoric  
580 fluids and carbonates alone may not be reconciled with the observed data. We  
581 argue that carbonates from the MEL site crystallized from the same meteoric fluid  
582 but at higher temperatures. These fluids percolated through conduits that allowed  
583 them to reach deeper parts of the crust and return to shallow crustal levels without  
584 losing much heat. Compared to thrust systems alone, thrust followed by strike-  
585 slip and extensional faulting may provide deep fluid conduits. Based on hydrogen  
586 isotopes, Nesbitt and Muehlenbachs (1989) concluded that the tectonic regime

587 might drastically control the depth of fluid interaction in the crust. This  
588 interpretation also agrees with previous studies based on fluid inclusions and  
589 sulfur isotope geothermometry performed in the MEL site area ([Misi and Kyle](#)  
590 [1994](#), [Misi, Iyer et al. 1999](#), [Misi, Iyer et al. 2005](#)), Fluid-rock interactions may  
591 also explain the presence of base metals in these high-temperature veins,  
592 suggesting that these chemical elements were scavenged from deeper crustal  
593 levels.

594 The role of deep crustal fluids at the MEL and MAM sites is further  
595 suggested by the petrographic and mineralogical features observed at these sites  
596 ([Fig. 8](#)). In addition to the high concentration of base metals (e.g., Pb, Zn, Fe),  
597 these sites display a pervasive replacement of the primary carbonates by silica.  
598 Silicification events are recognized as a diagenetic process in which Si-rich fluids  
599 affect a host rock, modifying its texture and mineralogy ([Menezes et al., 2019](#)).  
600 For example, [Haldar and Tisljer \(2014\)](#) documented a silicification process where  
601 opal/chalcedony/low-temperature quartz replaces calcite/aragonite/dolomite.  
602 The percolation of meteoric fluids at the deep crustal level provided the required  
603 conditions to mobilize silica at the MEL and MAM sites.

604 Deep meteoric fluid circulation along the Carfarnaun fault is comparable  
605 to other worldwide geological examples in which surface waters penetrate along  
606 tectonic structures. For instance, based on the Friedman and O'Neil (1977)  
607 isotope fractionation diagram, [Mozafari et al. \(2015\)](#) reconstructed the  
608 composition of the parent fluids that were in equilibrium with the vein infill in the  
609 Jabal Qusaybah Anticline (Adam Foothills, North Oman). The authors discussed  
610 a paleofluid evolutionary model related to the deformation front of the foreland  
611 fold and thrust belt. The strike-slip tectonic regime introduces a different type of  
612 fluid flow linked to the fault zone. The shifts in the stable isotope values forming



613 different fields with comparable values (Fig. 12) possibly originate from different  
614 phases of strike-slip movement. A similar spread in the fluid inclusion isotope  
615 ratios was discussed by de Graaf et al. (2020) after analyzing the wide variety of  
616 vein-type mineralization caused by deep-seated brines in the Hartz Mountains,  
617 Germany. Other studies examined the complex recrystallization processes along  
618 dolomitization fronts causing dissolution of the host limestones and precipitation  
619 of dolomite crystal structures depending on the porosity-permeability properties  
620 of the sediments present in the fault systems (Koeshidayatullah et al., 2020).

621         Similar to the Cafarnaun fault, the interplay between tectonics and fluid  
622 circulation has played a major role in the evolution of the inner Northern  
623 Apennines. As shown by Brogi et al. (2020), active transfer zones associated  
624 with an extensional tectonism control the deposition of travertine deposits by  
625 enhancing fluid circulation. Other studies in the same area have shown that  
626 these trending faults have also controlled the development of magmatic activities  
627 (Brogi et al., 2021) and Hg-Sb ore deposits (Brogi et al., 2011), further  
628 suggesting that these structures may connect different geological systems and  
629 play a major role in the remobilization of chemical constituents. They also  
630 indicate that competition between crustal stretching and surface uplift  
631 continuously switches the local intermediate stress axis, thus promoting quick  
632 changes in the direction of the maximum permeability (Liotta and Brogi, 2020).  
633 These changes further promote lateral and vertical migration of fluids within the  
634 system.

635

## 636 **6. Conclusion**

637         This study in the São Francisco Craton focuses on the hydrothermal  
638 activity in the Cafarnaun fault and its host rock and yields the following

639 conclusions. The São Francisco Craton is a cold and thick block preserved from  
640 deformation in the Brasiliano orogeny (740-580 Ma). However, a few tectono-  
641 thermal events affected the Craton along its boundary in Neoproterozoic times.  
642 One of these events was repeated hydrothermal activity along the Cafarnaum  
643 fault, a N-S-striking, 170 km long, strike-slip fault that juxtaposes Neoproterozoic  
644 carbonate units and Mesoproterozoic siliciclastic-carbonate units in the northern  
645 part of the Craton.

646         Hydrothermal boiling and implosive brecciation occurred along the fault.  
647 Decompression and cooler conditions induced precipitation of hydrothermal  
648 minerals in N-W-striking dilational jogs, mainly flanking the northern and southern  
649 fault terminations. The hydrothermal fluid structures are composed of  
650 hydrothermal breccias close to the main fault zones and along dilational jogs. In  
651 addition, calcite veins in the host units away from the fault are also part of the  
652 hydrothermal system. Therefore, the geometry of faults at shallow crustal levels  
653 influences the location of hydrothermal deposits.

654         Based on isotopic geochemistry, we show that meteoric water was the  
655 main fluid source that percolated the sedimentary rocks of the Irecê Basin and  
656 the Cafarnaum fault zone. Fluid inclusions in carbonate veins from the central  
657 part of the basin indicate a meteoric fluid with a  $\delta D$  value near -45‰ and a  $\delta^{18}O$   
658 value near -6.5‰. Temperature estimates based on the oxygen isotopic  
659 fractionation between the carbonate veins from the central part of the basin and  
660 the trapped fluid inclusions indicate temperatures ranging between 40 and 70°C.  
661 These temperature conditions agree with the lower  $\delta^{18}O$  values of veins  
662 compared to the carbonate host rock. A similar  $\delta^{18}O$  fluid value (-6.5‰) is  
663 obtained based on the interaction between these fluids and carbonates from the  
664 lower and upper parts of the succession.

665 In contrast, carbonates at the front edges of the basin associated with the  
666 Cafarnaum fault exhibit much lower  $\delta^{18}\text{O}$  values, indicating higher crystallization  
667 temperatures. These carbonates are also associated with base metals and silica-  
668 rich fluids, suggesting that the fault behaved as a conduit for deeper fluid  
669 circulation in the basement. The mineral paragenesis (e.g., galena, sphalerite,  
670 barite, chlorite, illite, and quartz) and brecciated features associated with the  
671 veins and fault support this interpretation.

672

### 673 **Acknowledgements**

674 We thank Precambrian Research editor Victoria Pease and two anonymous  
675 reviewers for the positive criticism that greatly improved the study. This work is  
676 part of the first author PhD research work. This work was partially sponsored by  
677 Petrobras/UnB/UFRN (CristalDOM Project, coordinated by FHB – UFRN and  
678 CLC – Petrobras). We thank the Brazilian Agency of Oil, Gas, and Biofuels  
679 (Agência Nacional do Petróleo, Gas e Biocombustíveis, ANP).

680

### 681 **References**

- 682 Alsop, G.I., Weinberger, R., Marco, S., Levi, T., 2020. Bed-parallel slip: Identifying  
683 missing displacement in mass transport deposits. *J. Struct. Geol.* 131.  
684 <https://doi.org/10.1016/j.jsg.2019.103952>
- 685 Arancibia, G., Fujita, K., Hoshino, K., Mitchell, T.M., Cembrano, J., Gomila, R.,  
686 Morata, D., Faulkner, D.R., Rempe, M., 2014. Hydrothermal alteration in an  
687 exhumed crustal fault zone: Testing geochemical mobility in the Caleta  
688 Coloso Fault, Atacama Fault System, Northern Chile. *Tectonophysics* 623,  
689 147–168. <https://doi.org/10.1016/j.tecto.2014.03.024>
- 690 Bellot, J.P., 2008. Hydrothermal fluids assisted crustal-scale strike-slip on the  
691 Argentat fault zone. *Tectonophysics* 450, 21–33.  
692 <https://doi.org/10.1016/j.tecto.2007.12.009>
- 693 Bense, V.F., Gleeson, T., Loveless, S.E., Bour, O., Scibek, J., 2013. Fault zone  
694 hydrogeology. *Earth-Science Rev.* 127, 171–192.  
695 <https://doi.org/10.1016/j.earscirev.2013.09.008>

- 696 Bjørlykke, K., Egeberg, P.K., 1993. Quartz cementation in sedimentary basins.  
697 Am. Assoc. Pet. Geol. Bull. 77, 1538–1548.  
698 <https://doi.org/10.1306/bdff8ee8-1718-11d7-8645000102c1865d>
- 699 Brito, D.C., 2008. Geologia, Petrografia e Litogeoquímica dos Diques Máficos  
700 que ocorrem na porção sudeste da Chapada Diamantina, Bahia, Brasil.  
701 Master Degree thesis, Instituto de Geociências, Universidade Federal da  
702 Bahia, Brazil, 107p.
- 703 Brito Neves, B.B., Fuck, R.A., Pimentel, M.M., 2014. The Brasiliano collage in  
704 South America: A review. Brazilian J. Geol. [https://doi.org/10.5327/Z2317-](https://doi.org/10.5327/Z2317-4889201400030010)  
705 [4889201400030010](https://doi.org/10.5327/Z2317-4889201400030010)
- 706 Brito Neves, B.B., Dos Santos, R.A., Da Cruz Campanha, G.A., 2012. A  
707 discordância angular e erosiva entre os grupos Chapada Diamantina e  
708 Bambuí (Una) na folha Mirangaba-Bahia. Geol. USP - Ser. Cient. 12, 99–  
709 114. <https://doi.org/10.5327/Z1519-874X2012000200007>
- 710 Brogi A., Caggianelli A., Liotta D., Zucchi M., Spina A., Capezzuoli E., Casini A.  
711 and Buracchi E. (2021) The Gavorrano Monzogranite (Northern  
712 Apennines): An Updated Review of Host Rock Protoliths, Thermal  
713 Metamorphism and Tectonic Setting. Geosciences 11, 124.
- 714 Brogi A., Fabbrini L. and Liotta D. (2011) Sb–Hg ore deposit distribution  
715 controlled by brittle structures: The case of the Selvena mining district  
716 (Monte Amiata, Tuscany, Italy). Ore Geology Reviews 41, 35–48.
- 717 Brogi A., Liotta D., Capezzuoli E., Matera P. F., Kele S., Soligo M., Tuccimei P.,  
718 Ruggieri G., Yu T.-L., Shen C.-C. and Huntington K. W. (2020) Travertine  
719 deposits constraining transfer zone neotectonics in geothermal areas: An  
720 example from the inner Northern Apennines (Bagno Vignoni-Val d’Orcia  
721 area, Italy). Geothermics 85, 101763.
- 722 Byerlee, J., 1990. Friction, overpressure and fault normal compression. Geophys.  
723 Res. Lett. 17, 2109–2112. <https://doi.org/10.1029/GL017i012p0210Caine>,  
724 J.S., Bruhn, R.L., Forster, C.B., 2010. Internal structure, fault rocks, and  
725 inferences regarding deformation, fluid flow, and mineralization in the  
726 seismogenic Stillwater normal fault, Dixie Valley, Nevada. J. Struct. Geol. 32,  
727 1576–1589. <https://doi.org/10.1016/j.jsg.2010.03.004>
- 728 Calvin, W.M., Littlefield, E.F., Kratt, C., 2015. Remote sensing of geothermal-  
729 related minerals for resource exploration in Nevada. Geothermics 53, 517–  
730 526. <https://doi.org/10.1016/j.geothermics.2014.09.002>
- 731 Choi, J.H., Edwards, P., Ko, K., Kim, Y.S., 2016. Definition and classification of  
732 fault damage zones: A review and a new methodological approach. Earth-  
733 Science Rev. <https://doi.org/10.1016/j.earscirev.2015.11.006>
- 734 Choi, J.H., Edwards, P., Ko, K., Kim, Y.S., 2016. Definition and classification of  
735 fault damage zones: A review and a new methodological approach. Earth-  
736 Science Rev. <https://doi.org/10.1016/j.earscirev.2015.11.006>

- 737 Danderfer Filho, A., Lana, C.C., Nalini Júnior, H.A., Costa, A.F.O., 2015.  
738 Constraints on the Statherian evolution of the intraplate rifting in a Paleo-  
739 Mesoproterozoic paleocontinent: New stratigraphic and geochronology  
740 record from the eastern São Francisco craton. *Gondwana Res.* 28, 668–688.  
741 <https://doi.org/10.1016/j.gr.2014.06.012>
- 742 D'Angelo, T., Barbosa, M.S.C., Danderfer Filho, A., 2019. Basement controls on  
743 cover deformation in eastern Chapada Diamantina, northern São Francisco  
744 Craton, Brazil: Insights from potential field data. *Tectonophysics* 772.  
745 <https://doi.org/10.1016/j.tecto.2019.228231>
- 746 De Graaf, S., Lüders, V., Banks, D.A., Sośnicka, M., Reijmer, J.J.G., Kaden, H.  
747 and Vonhof, H.B. (2020) Fluid evolution and ore deposition in the Harz  
748 Mountains revisited: isotope and crush-leach analyses of fluid  
749 inclusions. *Mineralium Deposita*, 55, 47-62. [https://doi.org/10.1007/s00126-](https://doi.org/10.1007/s00126-019-00880-w)  
750 [019-00880-w](https://doi.org/10.1007/s00126-019-00880-w)  
751
- 752 Demarco, P.N., Masquelin, H., Prezzi, C., Aífa, T., Muzio, R., Loureiro, J., Peel,  
753 E., Campal, N., Sánchez Bettucci, L., 2020. Aeromagnetic patterns in  
754 Southern Uruguay: Precambrian-Mesozoic dyke swarms and Mesozoic  
755 rifting structural and tectonic evolution. *Tectonophysics* 789.  
756 <https://doi.org/10.1016/j.tecto.2020.228373>
- 757 Dong, Z., Tang, J., Unsworth, M., Chen, X., 2015. Electrical resistivity structure  
758 of the upper mantle beneath Northeastern China: Implications for rheology  
759 and the mechanism of craton destruction. *J. Asian Earth Sci.* 100, 115–131.  
760 <https://doi.org/10.1016/j.jseaes.2015.01.008>
- 761 Dooley, T. P., and G. Schreurs, 2012, Analogue modelling of intraplate strike-  
762 slip tectonics: A review and new experimental results: *Tectonophysics*  
763 574–575, 1–71, doi: [10.1016/j.tecto.2012.05.030](https://doi.org/10.1016/j.tecto.2012.05.030).  
764
- 765 Evans, J.P., Chester, F.M., 1995. Fluid–rock interaction and weakening of faults  
766 of the San Andreas system: inferences from San Gabriel fault-rock  
767 geochemistry and microstructures. *Journal of Geophysical Research*.  
768 100,13007–13020.
- 769 Ferguson, I.J., Jones, A.G., Chave, A.D., 2012. Case histories and geological  
770 applications, in: Chave, A.D., Jones, A.G. (Eds.), *The Magnetotelluric*  
771 *Method: Theory and Practice*. Cambridge University Press, New York, pp.  
772 480–544. <https://doi.org/10.1017/CBO9781139020138.012>.
- 773 Fossen, H., Rotevatn, A., 2016. Fault linkage and relay structures in extensional  
774 settings-A review. *Earth-Science Rev.*  
775 <https://doi.org/10.1016/j.earscirev.2015.11.014>
- 776 Friedman, I., O'Neil, J.R., 1977. Compilation of stable isotope fractionation  
777 factors of geochemical interest: U.S. Geological Survey, Bulletin 440, 1–12.  
778 <https://doi.org/10.3133/pp440KK>  
779
- 780 Gudmundsson, A., Fjeldskaar, I., Brenner, S.L., 2002. Propagation pathways and  
781 fluid transport of hydrofractures in jointed and layered rocks in geothermal  
782 fields. *J. Volcanol. Geotherm. Res.* 116, 257–278.  
783 [https://doi.org/10.1016/S0377-0273\(02\)00225-1](https://doi.org/10.1016/S0377-0273(02)00225-1)

- 784 Gudmundsson, A., 2007. Infrastructure and evolution of ocean-ridge  
785 discontinuities in Iceland. *J. Geodyn.* 43, 6–29.  
786 <https://doi.org/10.1016/j.jog.2006.09.002>
- 787 Gudmundsson, A., 2001. Fluid overpressure and flow in fault zones: Field  
788 measurements and models. *Tectonophysics* 336.  
789 [https://doi.org/10.1016/S0040-1951\(01\)00101-9](https://doi.org/10.1016/S0040-1951(01)00101-9)
- 790 Haldar, S.K., Tišljarić, J., 2014. Introduction to Mineralogy and Petrology,  
791 Introduction to Mineralogy and Petrology. Elsevier Inc.  
792 <https://doi.org/10.1016/C2012-0-03337-6>
- 793 Haneberg, W.C., Mozley, P.S., Moore, J.C., Goodwin, L.B., 1999. Faults and  
794 Subsurface Fluid Flow in the Shallow Crust. *Geophys. Monogr. Ser.* 113,  
795 222.
- 796 Hardebeck, J.L., Hauksson, E., 1999. Role of Fluids in Faulting Inferred from  
797 Stress Field Signatures. *Science.* 285, 236–  
798 239. <https://doi.org/10.1126/science.285.5425.236>.
- 799 Hausegger, S., Kurz, W., Rabitsch, R., Kiechl, E., Brosch, F.J., 2010. Analysis of  
800 the internal structure of a carbonate damage zone: Implications for the  
801 mechanisms of fault breccia formation and fluid flow. *J. Struct. Geol.* 32,  
802 1349–1362. <https://doi.org/10.1016/j.jsg.2009.04.014>
- 803 Jébrak, M., 1997. Hydrothermal breccias in vein-type ore deposits: A review of  
804 mechanisms, morphology and size distribution. *Ore Geol. Rev.* 12, 111–134.  
805 [https://doi.org/10.1016/S0169-1368\(97\)00009-7](https://doi.org/10.1016/S0169-1368(97)00009-7)
- 806 Katz, D.A., Eberli, G.P., Swart, P.K., Smith, L.B., 2006. Tectonic-hydrothermal  
807 brecciation associated with calcite precipitation and permeability destruction  
808 in Mississippian carbonate reservoirs, Montana and Wyoming. *Am. Assoc.*  
809 *Pet. Geol. Bull.* 90, 1803–1841. <https://doi.org/10.1306/03200605072>
- 810 Koeshidayatullah, A., Corlett, H., Stacey, J., Swart, P.K., Boyce, A. and Hollis,  
811 C. (2020) Origin and evolution of fault-controlled hydrothermal dolomitization  
812 fronts: A new insight. *Earth and Planetary Science Letters*, 541, 116291.  
813 <https://doi.org/10.1016/j.epsl.2020.116291>
- 814 Kuchenbecker, M., Reis, H.L.S., Fragoso, D.G.C., 2011. Caracterização  
815 Estrutural e Considerações sobre a evolução tectônica da Formação Salitre  
816 na porção central da Bacia de Irecê, norte do Cráton do São Francisco (BA).  
817 *Geonomos.* 19, 42–49. <https://doi.org/10.18285/geonomos.v19i2.40>.
- 818 La Bruna, V., Lamarche, J., Agosta, F., Rustichelli, A., Giuffrida, A., Salardon, R.,  
819 Marié, L., 2020. Structural diagenesis of shallow platform carbonates: Role  
820 of early embrittlement on fracture setting and distribution, case study of  
821 Monte Alpi (Southern Apennines, Italy). *J. Struct. Geol.* 131.  
822 <https://doi.org/10.1016/j.jsg.2019.103940>
- 823 La Bruna, V., Bezerra, F. H., Souza, V. H., Maia, R. P., Auler, A. S., Araujo, R.  
824 E., Cazarin, C. L., Rodrigues, M. A. F., Vieira L. C., Sousa, M. O. (2021).  
825 High-permeability zones in folded and faulted silicified carbonate rocks–  
826 Implications for karstified carbonate reservoirs. *Marine and Petroleum*  
827 *Geology* 128, 105046.

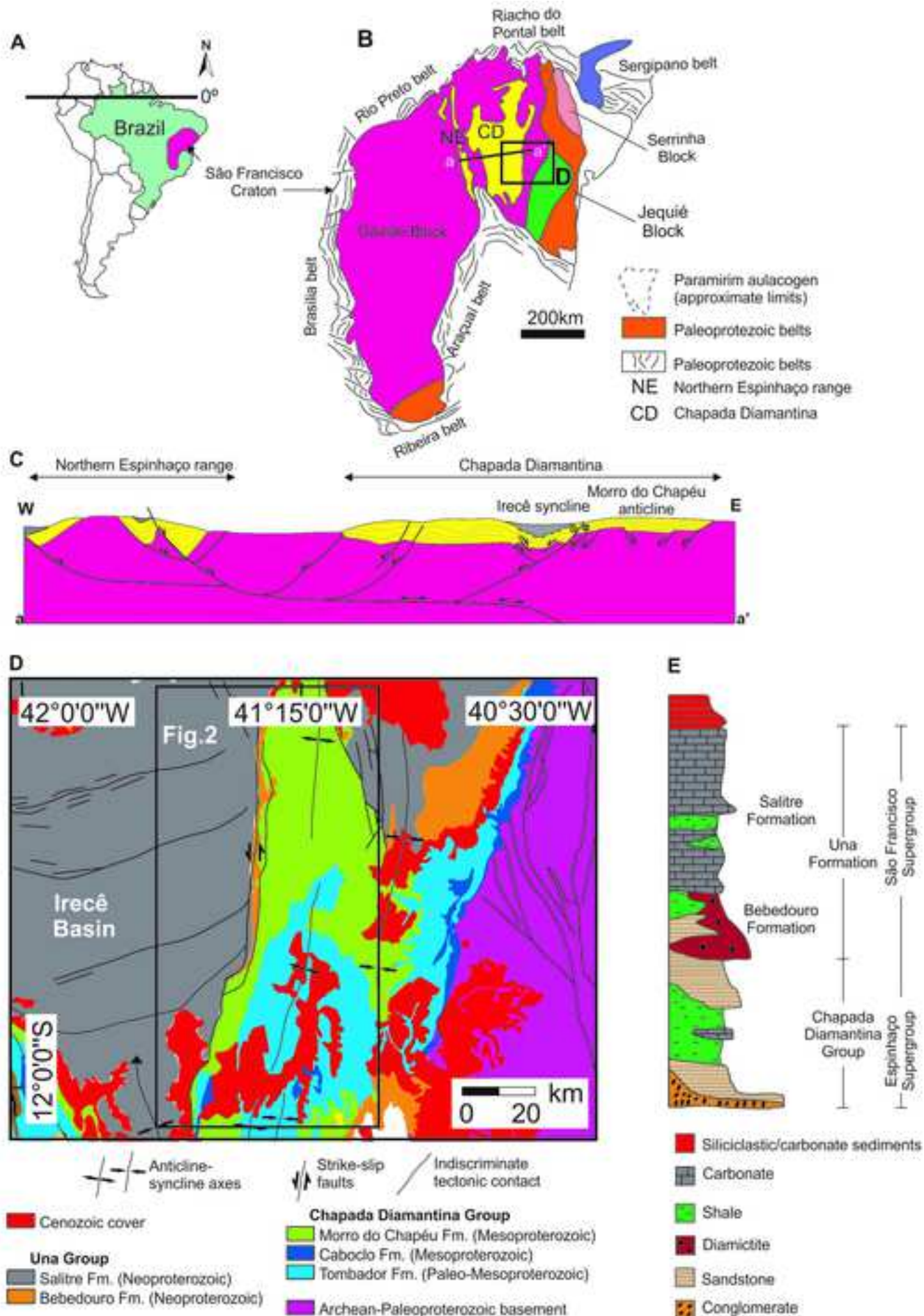
- 828 Lagoeiro, L.E., 1990. Estudo Da Deformação Nas Sequências Carbonáticas Do  
829 Grupo Una Na Região De Irecê, BA. Departamento de Geologia,  
830 Universidade Federal de Ouro Preto, Ouro Preto, MSc, thesis 105 p.
- 831 Liao, Z., Liu, H., Jiang, Z., Marfurt, K.J., Reches, Z., 2017. Fault damage zone at  
832 subsurface: A case study using 3D seismic attributes and a clay model  
833 analog for the Anadarko Basin, Oklahoma. *Interpretation* 5, T143–T150.  
834 <https://doi.org/10.1190/INT-2016-0033.1>
- 835 Liotta D. and Brogi A. (2020) Pliocene-Quaternary fault kinematics in the  
836 Larderello geothermal area (Italy): Insights for the interpretation of the  
837 present stress field. *Geothermics* 83, 101714.
- 838 Mapa Geológico do Estado da Bahia-CBPM/CPRM, 2003. Levantamento  
839 Aerogeofísico da Área do Centro Norte Bahia-CBPM, 2011/12.
- 840 Misi, A., Iyer, S.S.S., Coelho, C.E.S., Tassinari, C.C.G., Franca-Rocha, W.J.S.,  
841 de Abreu Cunha, I., Rocha Gomes, A.S., de Oliveira, T.F., Teixeira, J.B.G.,  
842 Filho, V.M.C., 2005. Sediment hosted lead-zinc deposits of the  
843 Neoproterozoic Bambuí Group and correlative sequences, São Francisco  
844 Craton, Brazil: A review and a possible metallogenic evolution model. *Ore*  
845 *Geol. Rev.* 26, 263–304. <https://doi.org/10.1016/j.oregeorev.2004.12.004>
- 846 Misi, A., Kaufman, A.J., Azmy, K., Dardenne, M.A., Sial, A.N., de Oliveira, T.F.,  
847 2011. Neoproterozoic successions of the São Francisco Craton, Brazil: The  
848 Bambuí, Una, Vazante and Vaza Barris/Miaba groups and their glaciogenic  
849 deposits. *Geol. Soc. Mem.* 36, 509–522. <https://doi.org/10.1144/M36.48>
- 850 Mozafari, M., Swennen, R., Balsamo, F., Clemenzi, L., Storti, F., El Desouky, H.,  
851 Vanhaecke, F., Tueckmantel, C., Solum, J. and Taberner, C., 2015.  
852 Paleofluid Evolution In Fault-Damage Zones: Evidence From Fault-Fold  
853 Interaction Events In the Jabal Qusaybah Anticline (Adam Foothills, North  
854 Oman). *Journal of Sedimentary Research* 85, 1525-1551.  
855 <https://doi.org/10.2110/jsr.2015.95>
- 856 Nabavi, S.T., Alavi, S.A., Wibberley, C.A.J., Jahangiri, M., 2020. Normal fault  
857 networks and their spatial relationships in Plio-Quaternary sedimentary  
858 series: A case study in the Zanjan Depression, NW Iran. *J. Struct. Geol.* 136.  
859 <https://doi.org/10.1016/j.jsg.2020.104072>
- 860 Ngwenya, B.T., Elphick, S.C., Main, I.G., Shimmield, G.B., 2000. Experimental  
861 constraints on the diagenetic self-sealing capacity of faults in high porosity  
862 rocks. *Earth Planet. Sci. Lett.* 183, 187–199. [https://doi.org/10.1016/S0012-821X\(00\)00261-2](https://doi.org/10.1016/S0012-821X(00)00261-2)
- 864 Nooitgedacht, C.W., H.J.L. van der Lubbe, S. de Graaf, M. Ziegler, P.T.  
865 Staudigel, and J.J.G. Reijmer., 2021. Restricted Internal Oxygen Isotope  
866 Exchange in Calcite Veins: Constraints from Fluid Inclusion and Clumped  
867 Isotope-Derived Temperatures. *Geochimica et Cosmochimica Acta.* 297,  
868 24–39. <https://doi.org/10.1016/j.gca.2020.12.008>. Ostermeijer, G.A.,  
869 Mitchell, T.M., Aben, F.M., Dorsey, M.T., Browning, J., Rockwell, T.K.,  
870 Fletcher, J.M., Ostermeijer, F., 2020. Damage zone heterogeneity on  
871 seismogenic faults in crystalline rock; a field study of the Borrego Fault, Baja  
872 California. *J. Struct. Geol.* 137. <https://doi.org/10.1016/j.jsg.2020.104016>.

- 873 Padilha, A.L., Vitorello, Í., de Pádua, M.B., Fuck, R.A., 2019. Magnetotelluric  
874 images of Paleoproterozoic accretion and Mesoproterozoic to  
875 Neoproterozoic reworking processes in the northern São Francisco Craton,  
876 central-eastern Brazil. *Precambrian Res.* 333.  
877 <https://doi.org/10.1016/j.precamres.2019.105416>
- 878 Peacock, D.C.P., Nixon, C.W., Rotevatn, A., Sanderson, D.J., Zuluaga, L.F.,  
879 2017a. Interacting faults. *J. Struct. Geol.* 97, 1–22.  
880 <https://doi.org/10.1016/j.jsg.2017.02.008>
- 881 Peacock, D.C.P., Dimmen, V., Rotevatn, A., Sanderson, D.J., 2017a. A broader  
882 classification of damage zones. *J. Struct. Geol.* 102, 179–192.  
883 <https://doi.org/10.1016/j.jsg.2017.08.004>
- 884 Peacock, D.C.P., Dimmen, V., Rotevatn, A., Sanderson, D.J., 2017b. A broader  
885 classification of damage zones. *J. Struct. Geol.* 102, 179–192.  
886 <https://doi.org/10.1016/j.jsg.2017.08.004>
- 887 Pedreira, A.J., Arcanjo, J.B., Oliveira, J.E., Silva, B.C.E., 1975. Projeto Bahia:  
888 Geologia Da Chapada Diamantina (Relatório Final). DNPM/CPRM,  
889 Salvador, Texto e Mapas. 182p.
- 890 Pessano, P.C., Ganade, C.E., Tupinambá, M., Teixeira, W., 2020. Updated map  
891 of the mafic dike swarms of Brazil based on airborne geophysical data. *J.*  
892 *South Am. Earth Sci.* 66. <https://doi.org/10.1016/j.jsames.2020.103076>
- 893 Pinto, L.G.R., de Pádua, M.B., Ussami, N., Vitorello, I., Padilha, A.L., Braitenberg,  
894 C., 2010. Magnetotelluric deep soundings, gravity and geoid in the south São  
895 Francisco craton: Geophysical indicators of cratonic lithosphere rejuvenation  
896 and crustal underplating. *Earth Planet. Sci. Lett.* 297, 423–434.  
897 <https://doi.org/10.1016/j.epsl.2010.06.044>
- 898 Pollard, D. D., Aydin, A. (1988). Progress in understanding jointing over the past  
899 century. *Geological Society of America Bulletin* 100(8), 1181-1204.
- 900 Pontes, C. C., Bezerra, F. H., Bertotti, G., La Bruna, V., Audra, P., De Waele,  
901 J., Auler, A. S., Balsamo, F., De Hoop, S., Pisani, L. (2021). Flow pathways in  
902 multiple-direction fold hinges: Implications for fractured and karstified  
903 carbonate reservoirs. *Journal of Structural Geology* 146, 104324. Rawling,  
904 G.C., Goodwin, L.B., Wilson, J.L., 2001. Internal architecture, permeability  
905 structure, and hydrologic significance of contrasting fault-zone types.  
906 *Geology* 29, 43–46. [https://doi.org/10.1130/0091-7613\(2001\)029<0043:IAPSAH>2.0.CO;2](https://doi.org/10.1130/0091-7613(2001)029<0043:IAPSAH>2.0.CO;2)
- 907
- 908 Rice, J.R., 1992. Fault Stress States, Pore Pressure Distributions, and the  
909 Weakness of the San Andreas Fault. *Int. Geophys.* 51, 475–503.  
910 [https://doi.org/10.1016/S0074-6142\(08\)62835-1](https://doi.org/10.1016/S0074-6142(08)62835-1)
- 911 Rozanski, K., Araguás-Araguás, L., & Gonfiantini, R., 1993. Isotopic patterns in  
912 modern global precipitation. Reference to a chapter in an edited book: P. K.  
913 Swart, K. C. Lohmann, J. McKenzie, & S. Savin, *Climate change in*  
914 *continental climate records, American physical union*, 78, pp. 1-36.
- 915 Sampaio A.R., Santos R.A., Rocha A.J.D., Guimarães J.T., 2001. Programa  
916 Levantamentos Geológicos Básicos do Brasil - PLGB. Jacobina, Folha



- 917 SC.24-Y-C, estado da Bahia. Escala 1:250.000. Brasília,  
918 CPRM/DIEDIG/DEPAT., p. 31.
- 919 Schwarz, E.J., Hood, P.J. and Teskey, D.J., 1987. Magnetic expression of  
920 Canadian diabase dykes and downward modelling. Reference to a chapter  
921 in an edited book: Halls, H.C. and Fahrig, W.F. (Eds.), Mafic Dyke Swarms.  
922 Geological Association of Canada, Special Paper,34, pp. 153–162.
- 923 Selway, K., 2014. On the Causes of Electrical Conductivity Anomalies in  
924 Tectonically Stable Lithosphere. *Surv. Geophys.* 35, 219–257.  
925 <https://doi.org/10.1007/s10712-013-9235-1>
- 926 Sibson, R. H., 1990. Faulting and fluid flow, in B. E. Nesbitt, ed., Short course on  
927 fluids in tectonically active regimes of the continental crust: Mineralogical  
928 Association of Canada Short Course Handbook, 18, pp. 93–131.
- 929 Sibson, R.H., 1987. Earthquake rupturing as a mineralizing agent in hydrothermal  
930 systems. *Geology* 15, 701–704. [https://doi.org/10.1130/0091-7613\(1987\)15<701:ERAAMA>2.0.CO;2](https://doi.org/10.1130/0091-7613(1987)15<701:ERAAMA>2.0.CO;2)
- 932 Sibson, R.H., Robert, F., Poulsen, K.H., 1988. High-angle reverse faults, fluid-  
933 pressure cycling, and mesothermal gold-quartz deposits. *Geology* 16, 551–  
934 555. [https://doi.org/10.1130/0091-7613\(1988\)016<0551:HARFFP>2.3.CO;2](https://doi.org/10.1130/0091-7613(1988)016<0551:HARFFP>2.3.CO;2)
- 935 Silveira, E.M., Söderlund, U., Oliveira, E.P., Ernst, R.E., Leal, A.B.M., 2013. First  
936 precise U-Pb baddeleyite ages of 1500Ma mafic dykes from the São  
937 Francisco Craton, Brazil, and tectonic implications. *Lithos* 174, 144–156.  
938 <https://doi.org/10.1016/j.lithos.2012.06.004>
- 939 Sleep, N.H., Blanpied, M.L., 1992. Creep, compaction and the weak rheology of  
940 major faults. *Nature* 359, 687–692. <https://doi.org/10.1038/359687a0>
- 941 Smeraglia, L., Giuffrida, A., Grimaldi, S., Pullen, A., La Bruna, V., Billi, A., Agosta,  
942 F., 2021. Fault-controlled upwelling of low-T hydrothermal fluids tracked by  
943 travertines in a fold-and-thrust belt, Monte Alpi, southern apennines, Italy. *J.*  
944 *Struct. Geol.* 144. <https://doi.org/10.1016/j.jsg.2020.104276>
- 945 Steyrer, H.P., Sturm, R., 2002. Stability of zircon in a low-grade ultramylonite and  
946 its utility for chemical mass balancing: The shear zone at Miéville,  
947 Switzerland. *Chem. Geol.* 187, 1–19. [https://doi.org/10.1016/S0009-2541\(02\)00010-4](https://doi.org/10.1016/S0009-2541(02)00010-4)
- 949 Souza, J. D. D., Melo, R. C. D., & Kozin, M., 2003. Mapa geológico do Estado da  
950 Bahia. Escala 1 : 1.000.000. CPRM/CBPM.
- 951 Taillefer, A., Soliva, R., Guillou-Frottier, L., Goff, E. Le, Martin, G., Seranne, M.,  
952 2017. Fault-related controls on upward hydrothermal flow: An integrated  
953 geological study of the têt fault system, Eastern Pyrénées (France).  
954 *Geofluids* 2017. <https://doi.org/10.1155/2017/8190109>
- 955 Teixeira, J.B.G., Misi, A., Da Silva, M.D.G., De Brito, R.S.C., 2019.  
956 Reconstruction of precambrian terranes of northeastern Brazil along  
957 cambrian strike-slip faults: A new model of geodynamic evolution and gold  
958 metallogeny in the State of Bahia. *Brazilian J. Geol.* 49.  
959 <https://doi.org/10.1590/2317-4889201920190009>

- 960 Teixeira, W., Oliveira, E.P., Marques, L.S., 2017. Nature and Evolution of the  
961 Archean Crust of the São Francisco Craton, in: Heilbron, M., Cordani, U.G.,  
962 Alkmim, F.F. (Eds.), São Francisco Craton, Eastern Brazil: Tectonic  
963 Genealogy of a Miniature Continent. Springer, Cham, pp. 29–56.doi:  
964 10.1007/978-3-319-01715-0\_3.
- 965 Thiel, S., Heinson, G., 2013. Electrical conductors in Archean mantle-Result of  
966 plume interaction? *Geophys. Res. Lett.* 40, 2947–2952.  
967 <https://doi.org/10.1002/grl.50486>
- 968 Wibberley, C.A.J., Shipton, Z.K., 2010. Fault zones: A complex issue. *J. Struct.*  
969 *Geol.* <https://doi.org/10.1016/j.jsg.2010.10.006>
- 970 Yilmaz, T.I., Prosser, G., Liotta, D., Kruhl, J.H., Gilg, H.A., 2014. Repeated  
971 hydrothermal quartz crystallization and cataclasis in the Bavarian Pfahl  
972 shear zone (Germany). *J. Struct. Geol.* 68, 158–174.  
973 <https://doi.org/10.1016/j.jsg.2014.09.004>
- 974 Zhang, S., Tullis, T.E., Scruggs, V.J., 2001. Implications of permeability and its  
975 anisotropy in a mica gouge for pore pressures in fault zones. *Tectonophysics*  
976 335, 37–50. [https://doi.org/10.1016/S0040-1951\(01\)00044-0](https://doi.org/10.1016/S0040-1951(01)00044-0).
- 977
- 978



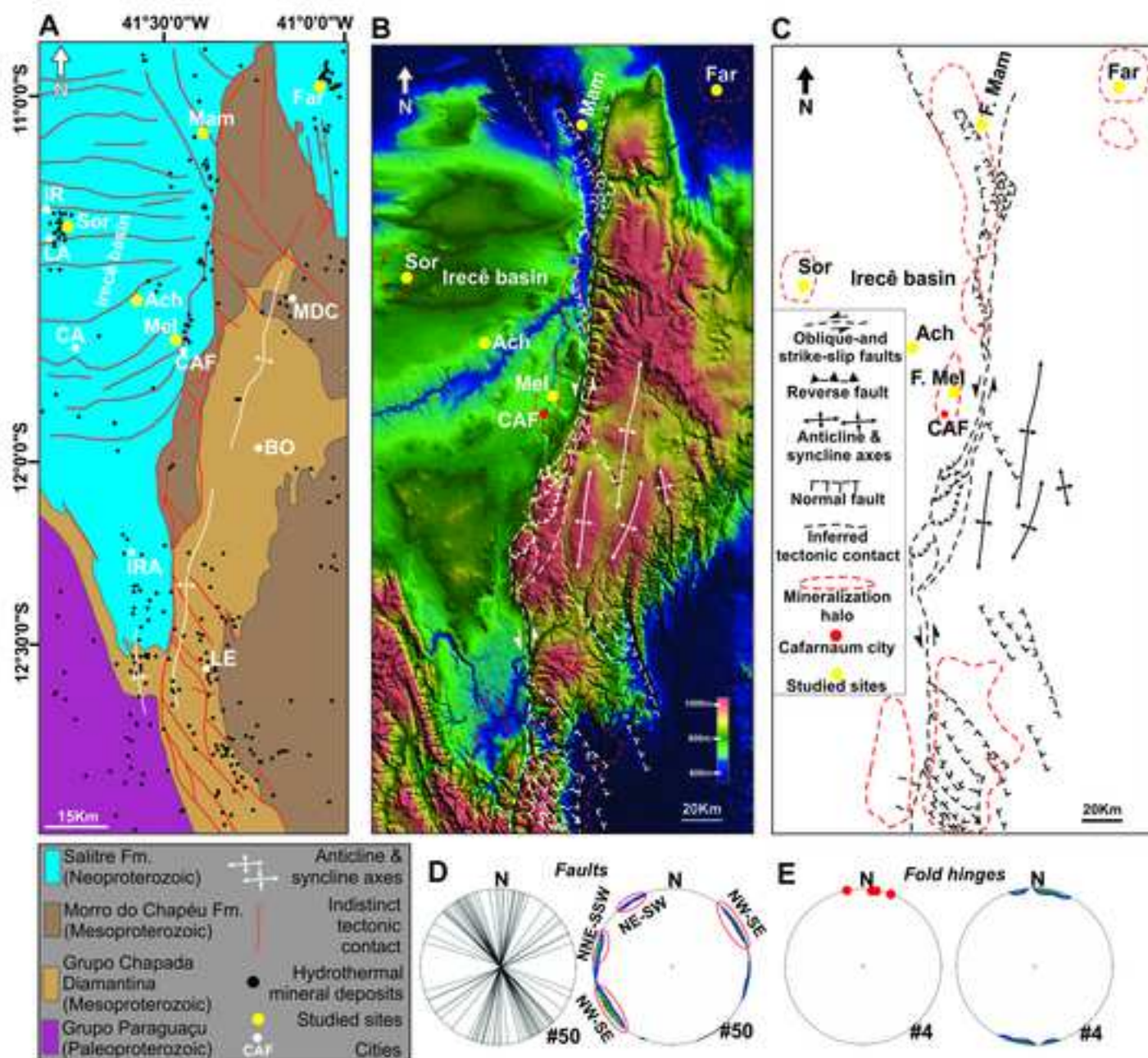


Figure 2. (A) Simplified geological map modified after *Levantamento Aerogeofísico da Área de Centro Norte Bahia - CBPM, 2011/12 Geologia - Mapa Geológico do Estado da Bahia - CBPM/CPRM, 2003*. (B) Structural framework of the study area superposed on ALOS PALSAR imagery. Dashed lines represent the inferred faults. Continuous white lines represent both anticline and syncline axes. (C) Line drawing of the structural framework presented in B. (D) Lower hemisphere equal-area projections of great circles representing the attitude of the documented faults and equal-area projection/density contour plots of the poles of the measured faults. (E) Lower hemisphere equal-area projections of fold hinges and relative density contour plots. (the map location can be found in Fig. Geological map).

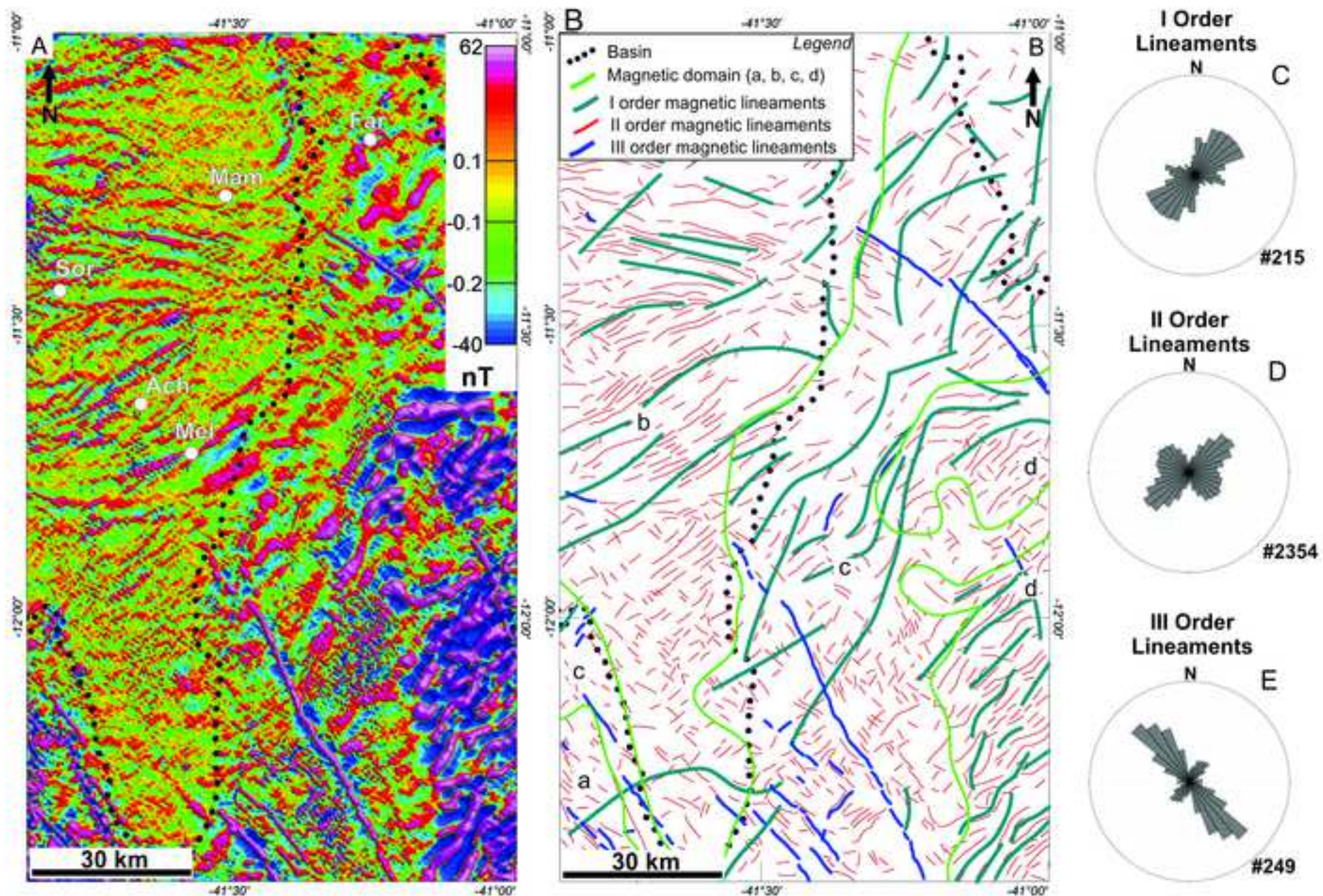


Figure 3. Behavior of magnetic lineaments in the study area: (A) Map of first derivative. (B) Lineaments Line drawing of the map presented in A. (C-D-E) Rose diagram representing the attitude of the documented first, second and third order lineaments.

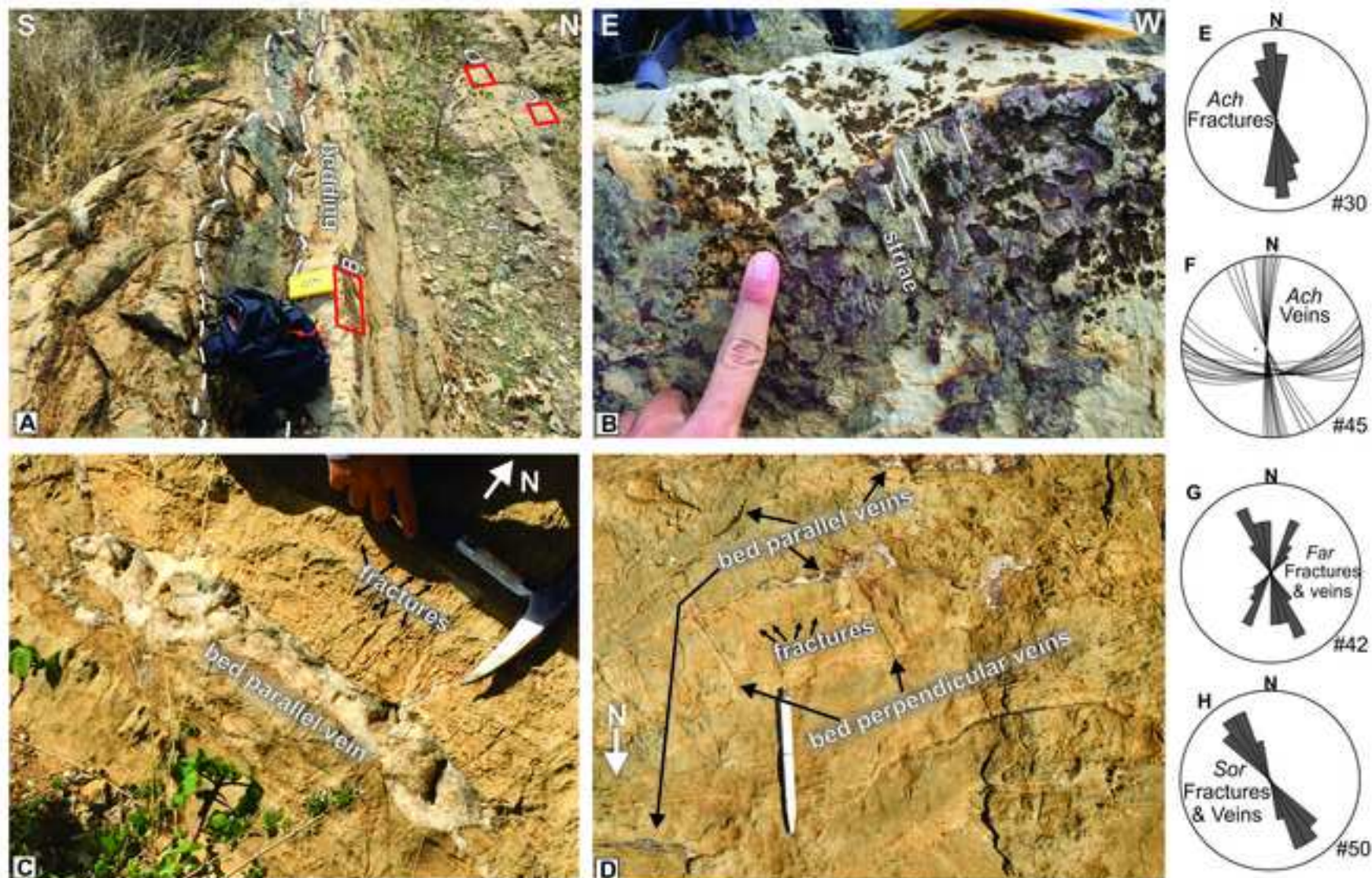


Figure 4. (A) Outcrop view of subvertical bed layers in the Achado outcrop; (B) Close up view of a bed parallel slip surface. Kinematic indicators, such as striae are visible along the slip surface. (C) Close up view of a large bed parallel vein and bed perpendicular fractures; (D) Close up view of bed parallel veins and bed perpendicular fractures and veins. (E) Rose diagram of the documented fractures in the Ach outcrop. (F) Lower hemisphere equal area projection of veins measured in the Ach outcrop. (G) and (H) Rose diagram of the documented fractures and veins in the Far and Sor outcrops. See Fig. 2 for outcrops location.

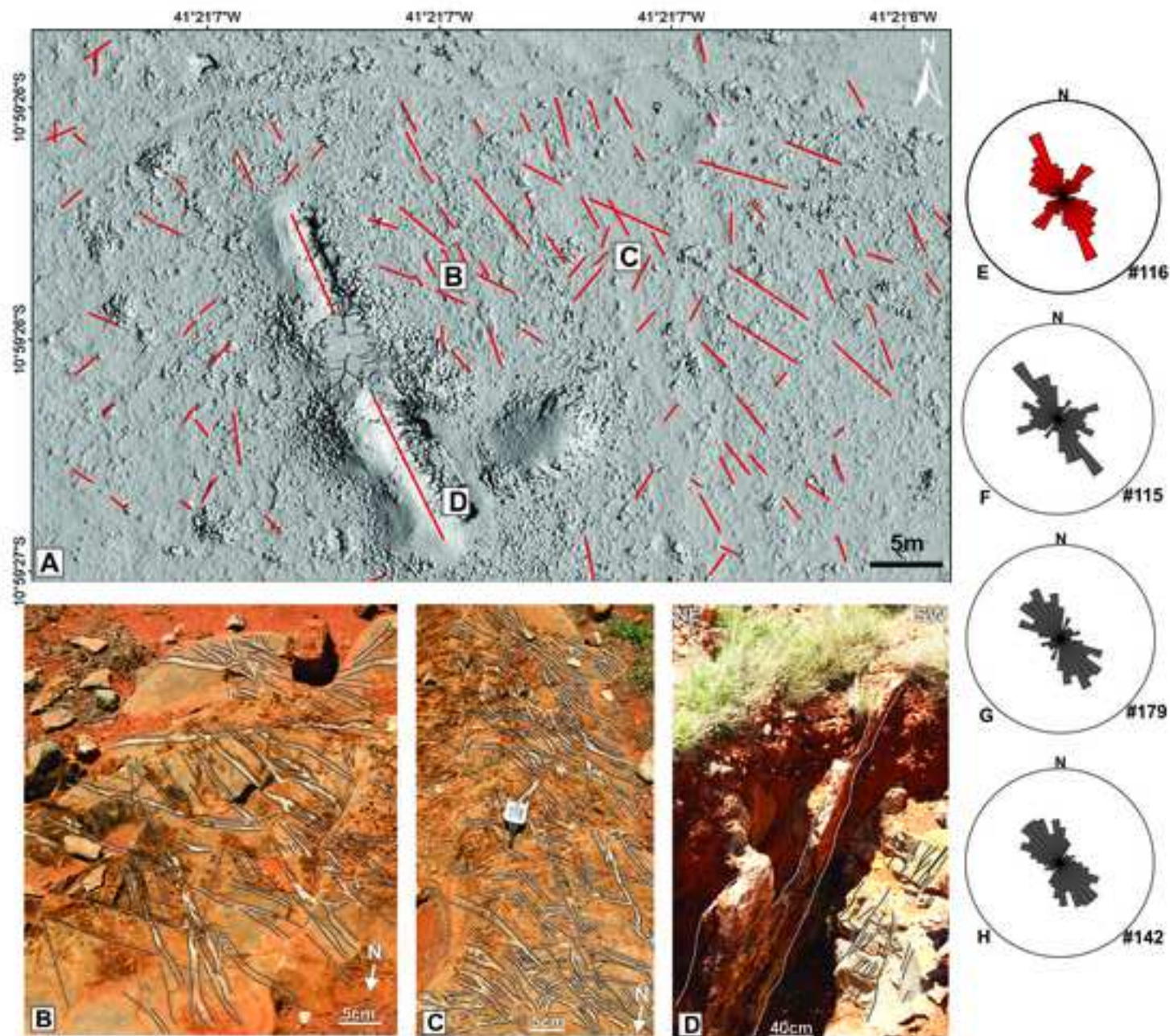


Figure 5. (A) Digital elevation model (DEM) of the Mammonas outcrop (outcrop localization in fig. 2. Mam). Red lines are associated to the structural lineaments; (B)(C) Outcrop view of veins and fractures. (D) Outcrop view of a large vein located in a fault damage zone. (E) Rose diagram of the identified structural features from the DEM in Fig. 5a; (F) Rose diagram of the documented veins and fractures displayed in Fig. 5b; (G) Rose diagram of the documented veins and fractures displayed in fig. 5c; (H) Rose diagram of the documented veins and fractures displayed in fig. 5d. See Fig. 3 for outcrops location.

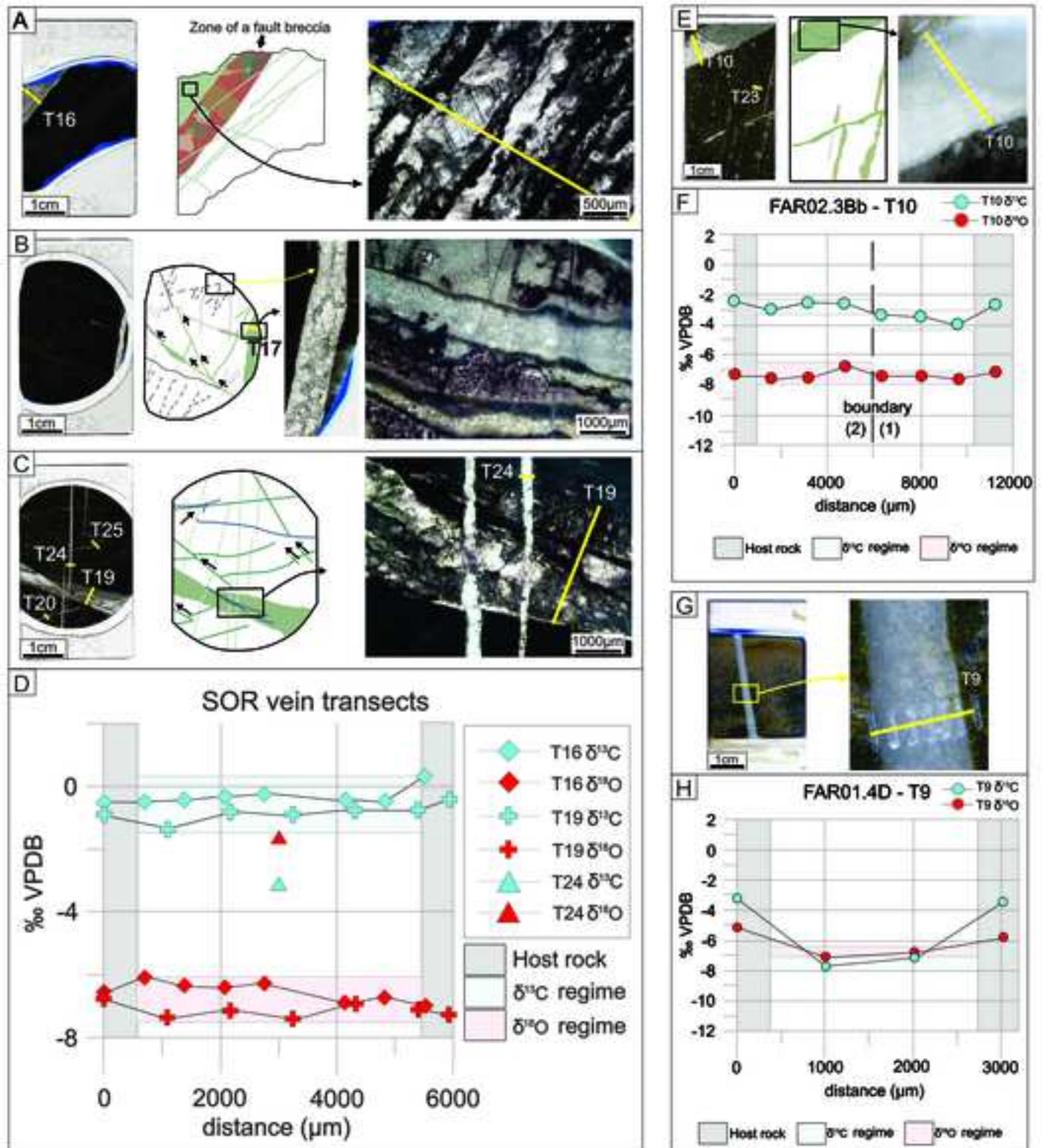


Figure 6. A) On the left, thin section SOR01.2Aa. On the center graphical representation of SOR01.2Aa with veins in green and fault breccia in multicolor. On the right, zoom in on sheeted character of vein T16. B) On the left, thin section SOR01.2Ab. On the center graphical representation of SOR01.2Ab. On the right zoom in on bedding parallel stylolites and N9E-SSW fractures. C) On the left, thin section SOR01.3Aa. On the center Micro map of all present features. On the right, crosscutting of shear fracture T19 and N-S vein T24. D) Stable isotope transects of T16, T19 and T24. E) Thin section FAR02.3Bb. On the center, graphic representation of thin section. On the left, zoom in on transect T10 across two calcite phases including crystallization. F) Transect T10. G) Thin section FAR01.4D, and zoom in on vein T9 with sampling location including crystallization. H) Transect T9.



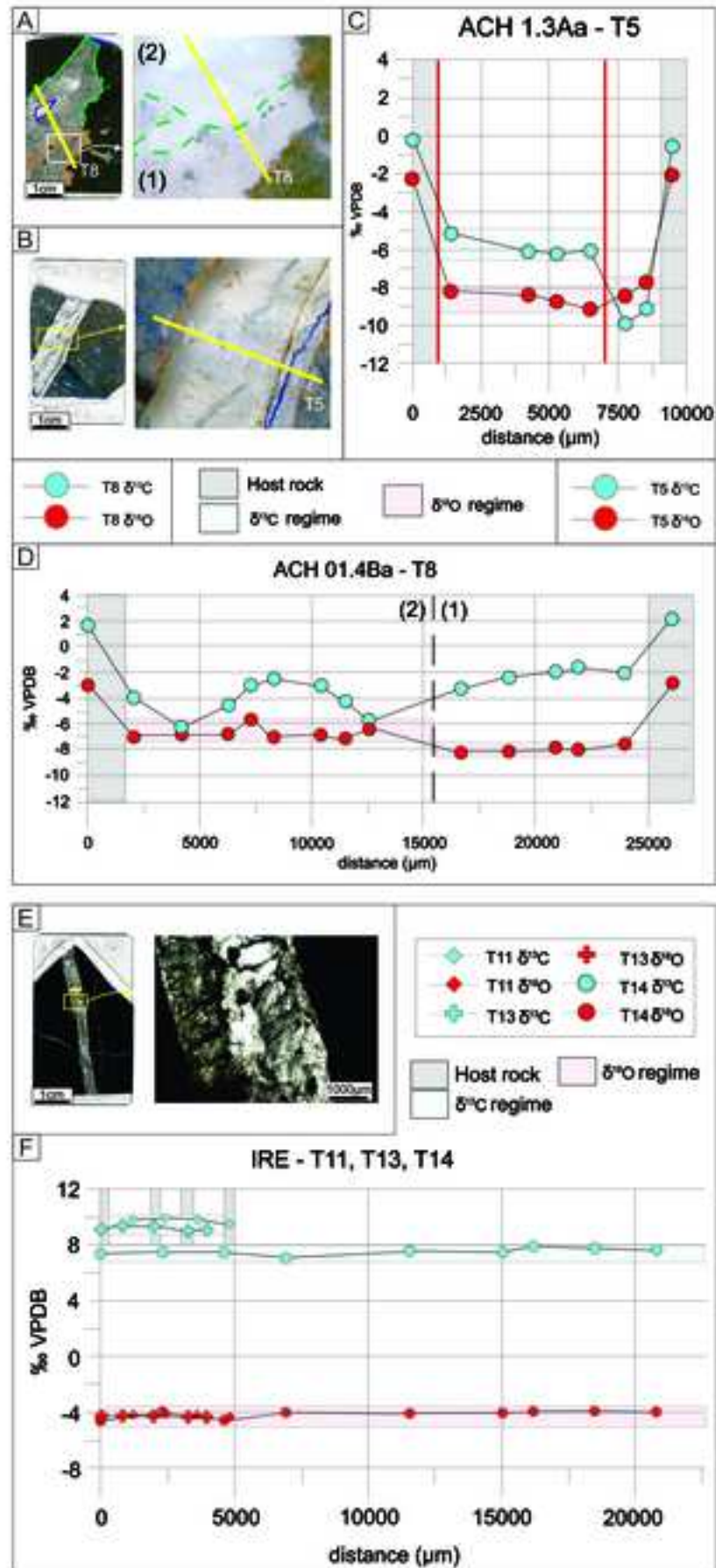


Figure 7. A) Thin section ACH01.4Ba with T8 location and two zones and, zoom in on zone boundary between (1) no host rock remnants and (2) with host rock remnants B) Thin section ACH01.3Aa and, zoom in on transect T5. C) Transect T5. The red lines mark a change in  $\delta^{13}\text{C}_{\text{VPDB}}$  and a new growth plane. D) Stable isotope transect of T8. Note the difference in  $\delta^{18}\text{O}$ . E) Thin section IRE01.2Aa, and, zoom in on vein infill with needle shaped anagorite remnants. F) Stable isotope transects of vein T11, T13 and T14 from IRE. Host rock and vein infill have an almost identical isotope composition.

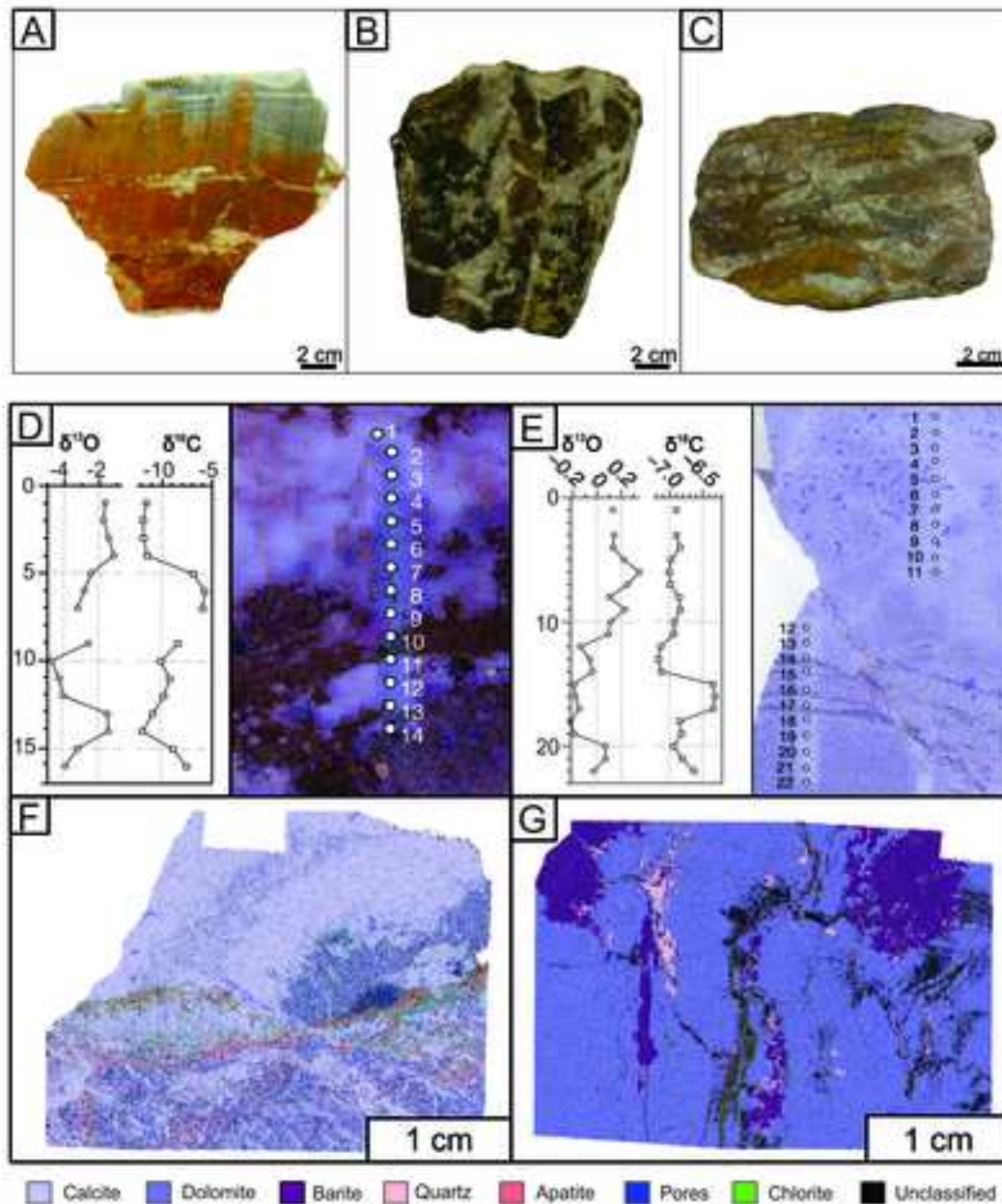


Figure 8. Samples from Melancias area showing the effects of hydrothermal alteration and hydraulic fracturing. A) Carbonate that shows partially preserved primary features grading to a brecciated zone. In the lower part of the sample, the primary features were obliterated by the hydrothermal alteration. B) Vein of carbonate by successive precipitation of carbonate and Fe-rich zones. C) Hydraulic breccia with clasts of the primary carbonate. D) and E) Thin section from Melancias in which calcite is the main mineral. The diagram also presents  $\delta^{13}\text{C}$  and  $\delta^{18}\text{O}$  across profiles. F) and G) QemScan image of samples from Melancias showing the hydrothermal mineralogy made of barite, quartz, illite, and chlorite. Note that these minerals concentrate along fractures.

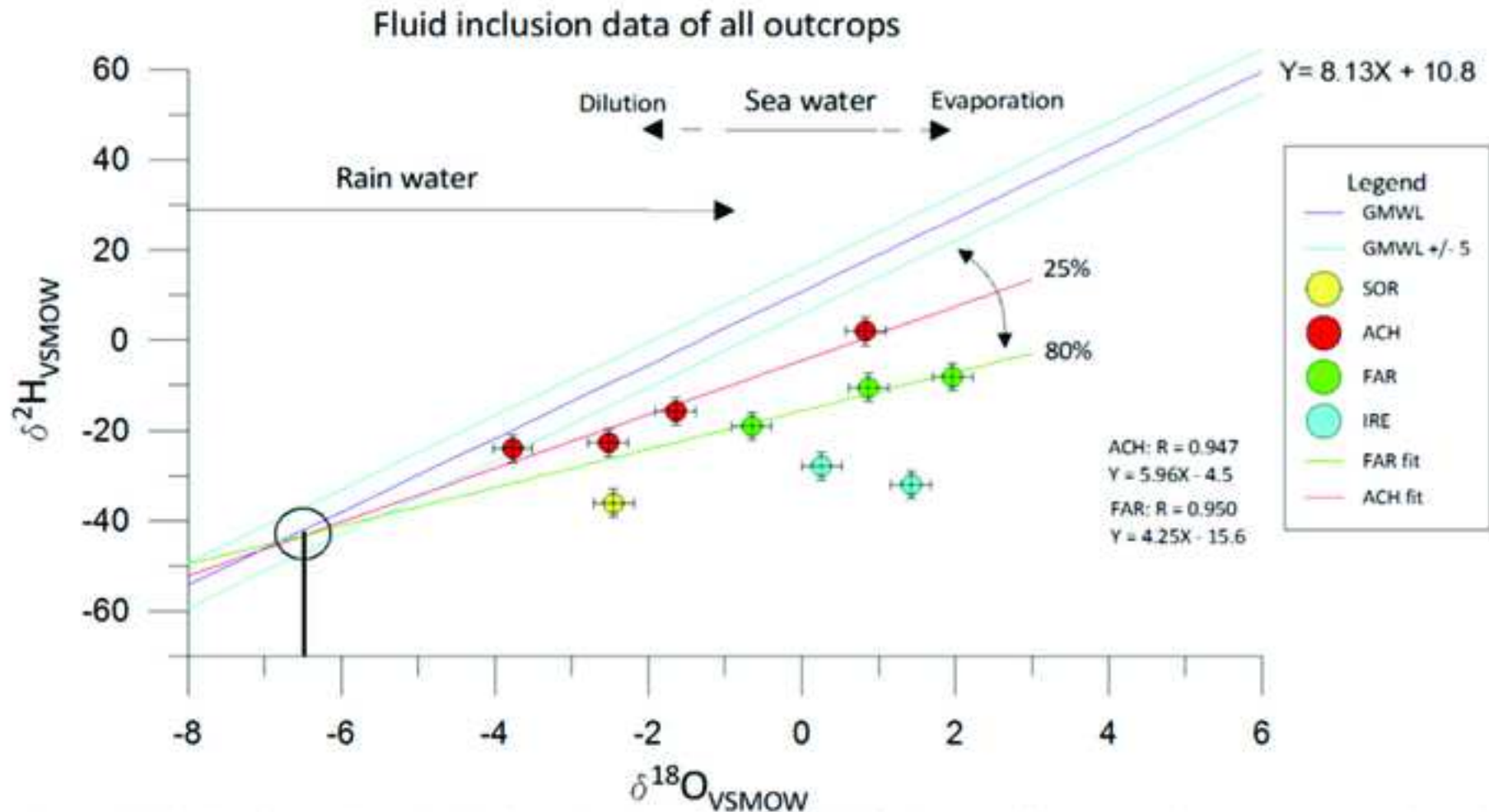


Figure 10. Fluid inclusion data GMWL based on Rozanski et al. (1993). Regions of marine and meteoric waters based on Moore (1989). Sample plot in both meteoric and marine domain. Trend lines of ACG and FAR cross the GMWL on the same point ( $\sim -6.5\text{‰}$  for  $\delta^{18}\text{O}_{\text{VSMOW}}$ ;  $-45\text{‰}$  for  $\delta\text{D}_{\text{VSMOW}}$ ).

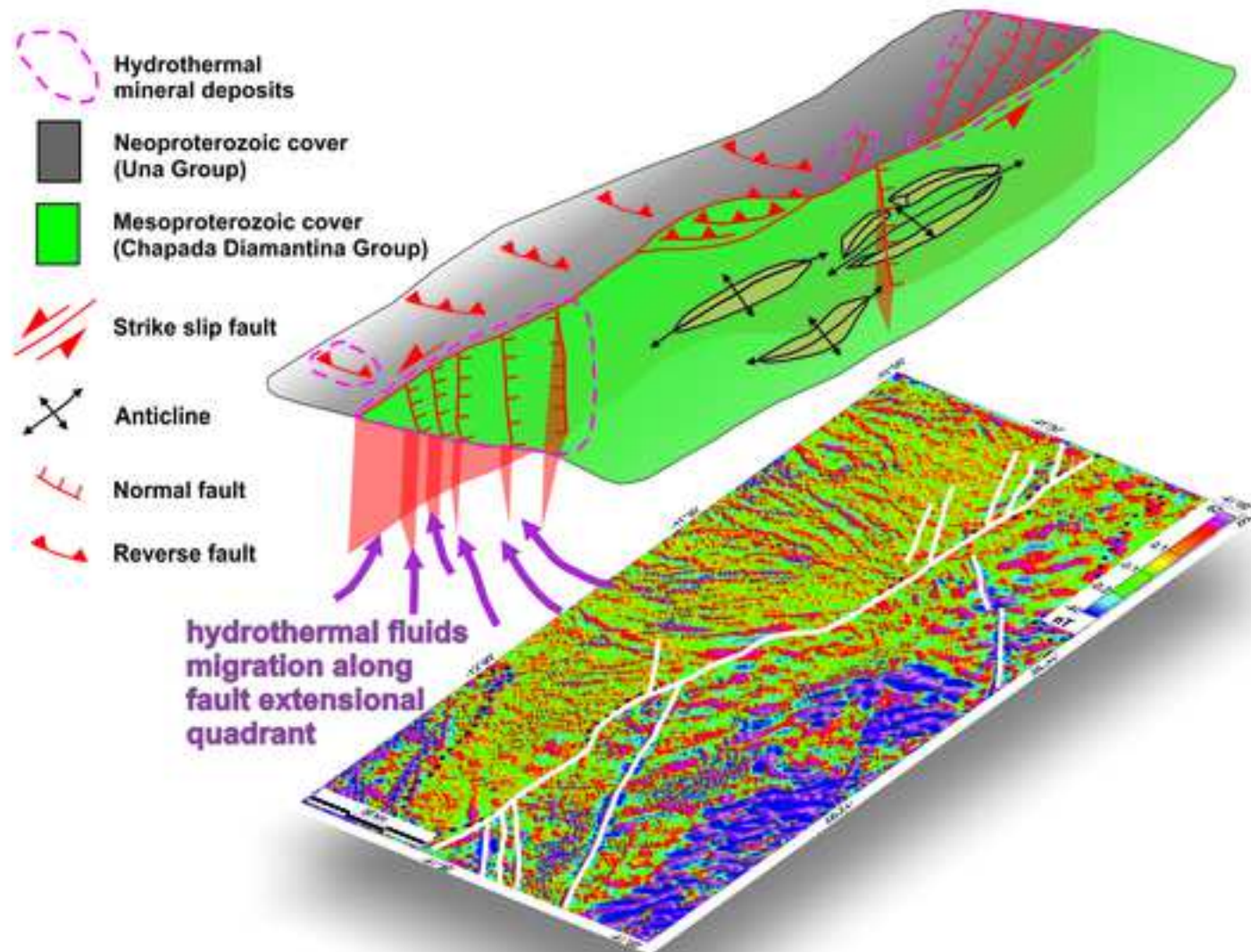


Figure 10. Conceptual model proposed for the study area. Cartoon displaying the current regional scale configuration and the connection with the deep magnetic lineaments.

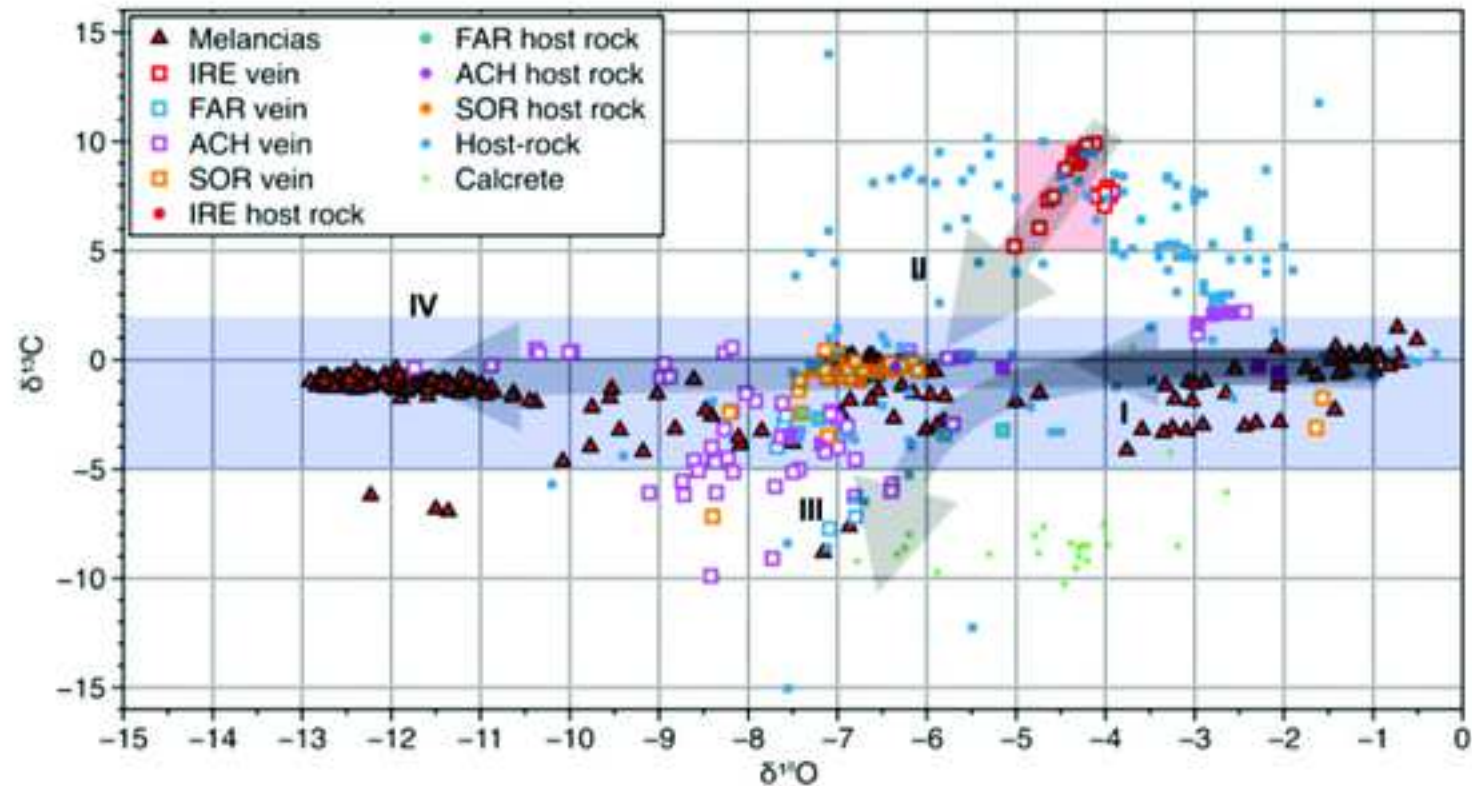


Figure 11. Carbon and oxygen isotopes of samples from the central part of the basin (IRE, FAR, ACH, and SOR) and samples from the Melancias outcrop compared to other published isotope data from the basin. This plot shows different scenarios of isotope evolution: I. Interaction between meteoric fluid and carbonates of the lower stratigraphic section; II. Interaction between meteoric fluid and carbonates of the upper stratigraphic section; III. Low  $d^{13}C$  carbonates related to the same fluids responsible for calcrete formation in the area; IV. Carbonates formed by high-temperature fluids that interacted with deep-crustal levels. Host-rock data (Misi and Kyle, 1994; Misi and Veizer, 1998; Borges et al., 2016; Caird et al., 2017); Calcrete data (Borges et al., 2016; Caird et al., 2017).



Table 2: Isotope data from fluid inclusions of carbonates from the central part of the basin. The temperature was calculated based on the oxygen isotopic composition of calcite and fluid, according to Kim & O'Neil (1997).

Sample	Location	Fluid $\delta D_{SMOW}$	Fluid $\delta^{18}O_{SMOW}$	Calcite $\delta^{18}O_{PDB}$	Calcite $\delta^{18}O_{SMOW}$	T in C
ACH01.2Bb T4-1	ACH	-22.7	-2.5	-7.4	23.3	39
ACH01.2Bb T4-2	ACH	-24.0	-3.8	-10.1	20.5	47
ACH01.3Aa T5-1 (left)	ACH	1.9	0.8	-8.6	22.1	66
ACH01.4BaT8-1 (grey)	ACH	-15.7	-1.6	-8.0	22.7	48
IRE01.2Aa T11	IRE	-32.0	1.4	-4.2	26.6	43
IRE01.3Ba T14	IRE	-27.9	0.3	-4.1	26.6	37
SOR01.3Aa T19	SOR	-36.0	-2.5	-6.5	24.3	35
FAR01.4D T9	FAR	-10.5	0.9	-7.0	23.7	56
FAR02.3Bb T10-1 (milky, right)	FAR	-8.2	2.0	-7.6	23.1	67
FAR02.3Bb T10-2 (transparent, left)	FAR	-19.0	-0.7	-7.5	23.1	51